Resonance Theory and Quantum Dynamics Simulations of Vibrational Polariton Chemistry

Wenxiang Ying^{1, a)} and Pengfei Huo^{1, 2, b)}

We present numerically exact quantum dynamics simulations using the hierarchical equation of motion (HEOM) approach to investigate the resonance enhancement of chemical reactions due to the vibrational strong coupling (VSC) in polariton chemistry. The results reveal that the cavity mode acts like a "ratepromoting vibrational (RPV) mode" that enhances the ground state chemical reaction rate constant when the cavity mode frequency matches the vibrational transition frequency. The exact simulation predicts that the VSC-modified rate constant will change quadratically as the light-matter coupling strength increases. When changing the cavity lifetime from the lossy limit to the lossless limit, the numerically exact results predict there will be a turnover of the rate constant. Based on the numerical observations, we present an analytic rate theory to explain the observed sharp resonance peak of the rate profile when tuning the cavity frequency to match the quantum transition frequency of the vibrational ground state to excited states. This rate theory further explains the origin of the broadening of the rate profile. The analytic rate theory agrees with the numerical results under the golden rule limit and the short cavity lifetime limit. To the best of our knowledge, this is the first analytic theory that is able to explain the sharp resonance behavior of the VSCmodified rate profile when coupling an adiabatic ground state chemical reaction to the cavity. We envision that both the numerical analysis and the analytic theory will offer invaluable theoretical insights into the fundamental mechanism of the vibrational strong coupling-induced rate constant modifications in polariton chemistry.

I. INTRODUCTION

Recent experiments^{1–5} have demonstrated that chemical kinetics can be enhanced^{4,5} or suppressed^{1–3,6} by coupling molecular vibrations to quantized radiation modes inside an optical microcavity. Note that in these experiments, there is no external influx of photons to the molecule-cavity hybrid system as the device is kept under a "dark" condition, and the change of the chemical rate constants is attributed to the formation of vibrational polaritons, quasiparticles of photon-vibrational excitation hybridization, as well as the vacuum field fluctuations.¹ This phenomenon is referred to as the vibrational strong coupling (VSC) enabled change of reactivities. A central feature of all VSC experiments is that when the cavity frequency ω_c is resonant to the bond vibration frequency ω_0 , *i.e.* when the following condition is satisfied

$$\omega_{\rm c} = \omega_0,\tag{1}$$

the reaction rate constant will be enhanced or suppressed, typically up to 4-5 times compared to the rate constants outside the cavity. If we define $|\nu_{\rm L}\rangle$ as the vibrational ground state of the reactant (left well), and $|\nu'_{\rm L}\rangle$ as the vibrationally excited state of the reactant, then ω_0 corresponds to the frequency of the $|\nu_{\rm L}\rangle \rightarrow |\nu'_{\rm L}\rangle$ transition. An experimental review summarizing the recent advances in VSC-modified chemical reactions can be found in Ref. 7,

whereas general discussions of this topic can be found in many recent reviews.⁸ This new strategy of VSC, if feasible, will allow one to bypass some intrinsic difficulties (such as intramolecular vibrational energy transfer) encountered in mode-selective chemistry that uses infrared (IR) excitation to tune chemical reactivities, offering a paradigm shift of synthetic chemistry through cavity-enabled bond-selective chemical transformations⁶, since one can use the cavity to selectively slow down one competing reaction over the target reactions.⁹

Unfortunately, a clear theoretical understanding of cavity-modified ground-state chemical reactivity remains missing, despite recent theoretical progress. ¹⁰ Currently, there are no well-accepted mechanisms or theoretical explanations for the observed phenomena. For electronically nonadiabatic reactions, such as electron transfer reactions coupled to optical cavities, there are numerous exciting progresses 11-13 which can explain the resonance effect (Eq. 1). Their relevance related to VSC experiments, which are all electronically adiabatic reactions, has yet to be clarified. 10 For the ground state adiabatic reaction coupled to the cavity, transition state theory (TST) predicts no modification of the rate constant 14-16 nor any significant cavity frequency dependence. 17 From Grote-Hynes (GH) theory, ^{18–20} it was conjectured that the cavity effect is purely from the modification of the transmission coefficients due to the dynamical caging effect^{9,21,22} (where the cavity mode acts as a regular nuclear vibration that provides friction to the reaction coordinate), providing a cavity frequency dependent VSC modification of the rate constants.

Despite the initial success of classical theories to ex-

¹⁾Department of Chemistry, University of Rochester, 120 Trustee Road, Rochester, New York 14627, USA

²⁾ The Institute of Optics, Hajim School of Engineering, University of Rochester, Rochester, New York 14627, USA

^{a)}Electronic mail: wying3@ur.rochester.edu

b) Electronic mail: pengfei.huo@rochester.edu

plain the cavity frequency, ω_c , dependence of VSC modifications, they often cannot predict the correct resonant frequency that matches the quantum vibration frequency ω_0 measured from the optical spectra. If one describes the rate constant using classical theory, such as the classical flux-side correlation function, 21 the Grote-Hynes (GH) theory, ^{21,22} the maximum modification of the rate constant occurs when $\omega_c \approx \omega_b$, where ω_b is the top of the barrier frequency (imaginary frequency of the Transition State). The Pollak-Grabert-Hänggi (PGH) theory, 23 or a semi-classical version of the quantum transition state theory (q-TST) rate theory, ²⁴ finds that the cavity-frequency dependent rate modification is related to either the top of the barrier frequency $\omega_{\rm b}$ (Eq. 21), the classical bottom of the well frequency $\omega_0^{\rm cl}$ (Eq. 26), or a broad frequency distribution between these two frequencies. For example, the GH theory for a double-well (DW) model in the spatial diffusion-limited regime (after the Kramers turnover) predicts²¹ that the VSC modification is sensitive to $\omega_{\rm b}$. The GH theory for a solvent-solute model coupled to the cavity predicts²² the VSC effect is sensitive to a frequency that depends on both $\omega_{\rm b}$ and $\omega_{\rm 0}^{\rm cl}$. The q-TST theory predicts²⁴ that the VSC-modified rate will have a broad profile that spans the range of $\omega_{\rm b}$ and $\omega_0^{\rm cl}$. The PGH theory for a DW system coupled to the cavity in the energy diffusion-limited regime (before the Kramers turnover) predicts that the rate modification could be closer to $\omega_0^{\rm cl}$ (see Fig. 5 of Ref. 23) or closer to $\omega_{\rm b}$ (see Fig. 2e of Ref. 25), due to the fact that the rate profile in this energy diffusion-limited regime is dominated by the energy loss process of the classical trajectory that travels between the bottom of the well and the top of the barrier. Related to the classical rate theory, a direct abinitio simulation²⁶ that investigates the reaction in Ref. 1 treats the electronic ground states ab-initially and treats nuclear and photonic degrees of freedom (DOFs) classically. The simulation suggests that the bond distance (of the reactive chemical bond) will be modified when the cavity frequency is close to either $\omega_{\rm b}$ or $\omega_0^{\rm cl}$ (note that this is not directly related to the rate constant).

Overall, in these classical/semi-classical rate theories, there is no knowledge directly related to the quantum vibrational ground and excited states and the associated transition frequency ω_0 , except for the pure harmonic potential that $\omega_0^{\rm cl} = \omega_0$. The only explicitly available frequencies are those $\omega_0^{\rm cl}$ and $\omega_{\rm b}$ that are directly related to the potential V(R) (Eq. 20). In this sense, the quantum vibration frequency ω_0 is intrinsically quantum information, as it is directly related to the vibrational eigenenergies (by solving the eigenequation and does not have a classical analogy when the potential energy surface is anharmonic). Interestingly, the purely classical description of the vibrational and photonic DOFs will provide different peak positions of the optical spectra and the rate modification profile. For example, as demonstrated in Ref. 25, the classical IR spectra of the molecule peaks at $\omega_0^{\rm cl}$ (because the classical trajectory predominantly samples the bottom of the well region), and the VSC-

modified rate profile peaks at $\omega_{\rm b}$, thus having a large frequency difference. Simply adding quantum statistics and quantum tunneling using ring polymer molecular dynamics (RPMD) will not produce the correct resonance frequency and sharp resonance²⁷ either because there is no explicit information of ω_0 in the ring polymer Hamiltonian. As also extensively discussed in Ref. 25, the exact quantum optical spectra and VSC-modified rate profile both peak at ω_0 , because they have a common origin related to the quantum transition of $|\nu_{\rm L}\rangle \rightarrow |\nu'_{\rm L}\rangle$. Our work confirms the same discovery²⁵ by treating $\hat{q}_{\rm c}$ as a bath DOF with spectral density description.

As such, experimental evidence strongly suggests that the VSC modification needs to be studied by treating the vibrational states quantum mechanically, such that the knowledge of ω_0 is included. The similarity of the optical profile of vibrational absorption and the cavitymodified rate constant also strongly suggests that both have a common origin, both of which correspond to the $|\nu_{\rm L}\rangle \rightarrow |\nu_{\rm L}'\rangle$ transition. This is because the optical transition is caused by $-\hat{\mu} \cdot E(t)$, where $\hat{\mu}$ is the transition dipole operator, and E(t) is the classical laser field, whereas the molecule-cavity coupling is caused by $\hat{\mu}(\hat{a}^{\dagger} + \hat{a}) \propto \hat{\mu} \cdot \hat{q}_{c}$, where \hat{a}^{\dagger} and \hat{a} are cavity field operators and $\hat{q}_c = \sqrt{\hbar/2\omega_c}(\hat{a}^{\dagger} + \hat{a})$ is the photonic coordinate that is proportional to the displacement field intensity inside the cavity.²⁸ Indeed, using the numerically exact hierarchical equations of motion $(HEOM)^{29-32}$ method to investigate the model reaction coupled to the cavity and by treating vibrational states and cavity Fock states quantum mechanically as the quantum subsystem, Reichman and co-workers in Ref. 25 indeed found resonance behavior of the rate profile, which is similar to the absorption spectra of the bare molecule outside the cavity (with similar features of narrow width and centered around ω_0). This numerically exact simulation provides invaluable insights into the mechanism of how the cavity modifies reaction rate constants. Nevertheless, an analytic theory to explain the VSC-enhanced rate constant is still missing.

In this work, we follow the inspiration from Ref. 25 and perform numerically exact simulations to investigate the VSC enhancement effect when coupling a single molecule inside a cavity. As opposed to the early work that treats the photonic DOF \hat{q}_c using Fock states and as part of the quantum subsystems, here, we use an effective spectral density theory to describe $\hat{q}_{\rm c}$ and cavity loss as an effective bath that couples to the reaction coordinate through the molecule-cavity interactions.³³ Because of the exact nature of HEOM, including \hat{q}_c inside the bath should not influence the description of quantum dynamics. This effective spectral density treatment not only provides computational efficiency (because the quantum subsystem is only the molecular reaction coordinate or equivalently the quantum vibrational states) that allows for a much faster convergence for the calculation but also provides an intuitive understanding of the cavity mode as a "ratepromoting vibration (RPV) mode", which will enhance

the rate constant if its frequency ω_c matches the transition frequency ω_0 . We found that the key mechanism lies in the population being pumped to the vibrationally excited state in the reactant well, which quickly tunnels to the vibrationally excited state in the product well and then relaxes to generate the vibrational ground state in the product well.

Based on these exact dynamics results, we further developed an analytic rate theory (Eq. 41), which is the central theoretical result of this work. Under the short cavity lifetime limit, $\tau_{\rm c} \to 0$, the rate reduces to an analytic answer in Eq. 44. We found that both the HEOM results and Fermi's Golden Rule (FGR) rate predict a resonant condition (Eq. 1) for the VSC-enhanced rate constant with a narrow width for the rate profile. The FGR rate theory predicts that the width of the VSCmodified rate profile is controlled by a convolution of two peaks: one with its width dictated by the nuclear vibrational broadening and the other with its width related to the cavity lifetime τ_c . Both HEOM results and the FGR rate constants predict that the rate enhancement will scale non-linearly with respect to the light-matter coupling strength (Eq. 48), resulting in a nonlinear scaling of the effective free energy barrier change (Eq. 50) if one chooses to interpret the VSC rate change entirely due to the change of effective free energy barrier (which is not a reasonable interpretation but has been widely used in experimental papers³). The current theory also predicts an interesting cavity lifetime dependence of the VSC modification on the rate constant. To the best of our knowledge, this is the first analytic rate theory to explain the adiabatic ground state chemical reaction modified by the VSC effect and to give a clear resonant behavior (Eq. 1). The interesting scaling of how the VSC rate constant will change by changing the light-matter coupling and cavity lifetime predicted by the current theory and the exact simulation encourages more experimental work to carefully study them, even with reactions that have already been reported. 1,4,5,7

II. MODEL HAMILTONIAN AND COMPUTATIONAL DETAILS

A. The Hamiltonian for Molecule-Cavity Hybrid System

We begin by introducing the Pauli-Fierz (PF) quantum electrodynamics (QED) Hamiltonian, which has been widely used to describe light-matter interactions in molecular cavity QED. We set $\hbar \equiv 1$ throughout this paper for convenience. Expressed in the dipole gauge and under the long-wavelength approximation, it is expressed as 21,34,35

$$\hat{H} = \frac{\hat{P}^2}{2M} + V(\hat{R}) + \frac{\hat{p}_c^2}{2} + \frac{\omega_c^2}{2} \left(\hat{q}_c + \sqrt{\frac{2}{\omega_c^3}} \chi \cdot \mu(\hat{R}) \right)^2 + \hat{H}_{\nu} + \hat{H}_c,$$
(2)

which is the PF QED Hamiltonian for the model used in this paper. Here, we include only the ground electronic state of the molecule. A detailed derivation of this Hamiltonian from the minimum-coupling Hamiltonian can be found in Ref. 21. In addition, $\hat{P}^2/2M$ is the kinetic energy of the nuclear DOF for the molecule, M is the effective mass of the nuclear vibration, $V(\hat{R})$ is the ground electronic state potential energy surface, and \hat{R} is the reaction coordinate. Further, $\hat{q}_c = \sqrt{1/(2\omega_c)}(\hat{a} + \hat{a}^\dagger)$ and $\hat{p}_c = i\sqrt{\omega_c/2}(\hat{a}^\dagger - \hat{a})$ are the photon mode coordinate and momentum operators, respectively, where \hat{a}^\dagger and \hat{a} are the photon mode creation and annihilation operators, and ω_c is the cavity frequency. Finally,

$$\chi = \sqrt{\omega_{\rm c}/(2\epsilon_0 \mathcal{V})} \,\hat{\mathbf{e}} \tag{3}$$

characterizes the light-matter coupling strength, where $\hat{\mathbf{e}}$ is the unit vector of the field polarization, ϵ_0 is the permittivity, and \mathcal{V} is the quantization volume inside the cavity. We also assume that the dipole moment is always aligned with the cavity polarization direction, such that $\chi \cdot \mu(\hat{R}) = \chi \cdot \mu(\hat{R})$, where $\chi \equiv \sqrt{\omega_c/(2\epsilon_0 \mathcal{V})}$.

Under the dipole gauge, the matter ground state permanent dipole moment $\mu(\hat{R})$ displaces the photon coordinate \hat{q}_c by the amount of $\sqrt{2/\omega_c^3} \chi \cdot \mu(\hat{R})$, which accounts for the light-matter interaction. Further, \hat{H}_{ν} is the dissipative system-bath Hamiltonian that describes the linear coupling between reaction coordinate \hat{R} and phonon bath, expressed as follows,

$$\hat{H}_{\nu} = \frac{1}{2} \sum_{i} \left[\hat{p}_{i}^{2} + \omega_{i}^{2} \left(\hat{x}_{i} - \frac{c_{i}}{\omega_{i}^{2}} \hat{R} \right)^{2} \right], \tag{4}$$

where the reorganization energy of the phonon (vibrational) environment is $\lambda_{\nu} \equiv \sum_{i} c_{i}^{2}/(2\omega_{i}^{2})$. Further, \hat{H}_{c} describes the loss of the cavity photon, through the noncavity modes $\{\tilde{x}_{j}\}$ that directly coupled to the cavity photon mode coordinate \hat{q}_{c} , expressed as follows,

$$\hat{H}_{c} = \frac{1}{2} \sum_{j} \left[\hat{p}_{j}^{2} + \tilde{\omega}_{j}^{2} \left(\hat{\tilde{x}}_{j} - \frac{\tilde{c}_{j}}{\tilde{\omega}_{j}^{2}} \hat{q}_{c} \right)^{2} \right].$$
 (5)

According to the Caldeira-Leggett system-bath model,³⁶ the baths as well as their coupling to the "system" can be described by spectral density functions, defined as

$$J_{\nu}(\omega) \equiv \frac{\pi}{2} \sum_{j} \frac{c_{j}^{2}}{\omega_{j}} \delta(\omega - \omega_{j}), \tag{6a}$$

$$J_{c}(\omega) \equiv \frac{\pi}{2} \sum_{i} \frac{\tilde{c}_{j}^{2}}{\tilde{\omega}_{j}} \delta(\omega - \tilde{\omega}_{j}), \tag{6b}$$

for molecular phonon and cavity photon-loss baths, respectively.

For simplicity, in this work, we assume that the dipole operator is linear, $\mu(\hat{R}) = \hat{R}^{37}$. As a result, the light-matter coupling term in Eq. 2 is simplified as $\sqrt{2\omega_c}\hat{q}_c\chi$.

 $\mu(\hat{R}) = \sqrt{2\omega_c}\chi\hat{q}_c\hat{R}$. Further, we define the normalized light-matter coupling strength,

$$\eta_{\rm c} = \frac{\chi}{\omega_{\rm c}} = \sqrt{\frac{1}{2\epsilon_0 \omega_{\rm c} \mathcal{V}}},\tag{7}$$

then the photon coordinate displacement in Eq. 2 becomes $\sqrt{2/\omega_c^3} \chi \cdot \mu(\hat{R}) \longrightarrow \sqrt{2/\omega_c} \eta_c \hat{R}$. The total Hamiltonian in Eq. 2 then becomes

$$\hat{H} = \frac{\hat{P}^2}{2M} + V(\hat{R}) + \frac{\hat{p}_c^2}{2} + \frac{\omega_c^2}{2} \left(\hat{q}_c + \sqrt{\frac{2}{\omega_c}} \eta_c \hat{R} \right)^2 + \hat{H}_{\nu} + \hat{H}_c.$$
(8)

To solve the quantum dynamics of Eq. 8, we plan to describe the reaction coordinate \hat{R} quantum mechanically, through its vibrational eigenstates, and everything else as the "bath" DOF through the corresponding exact quantum description.

B. The Effective Spectral Density Theory

The key idea in this paper is to establish a simple system-bath model described by an effective spectral density function without explicitly taking the photon DOF, \hat{q}_c , into the description of the quantum subsystem (such as through Fock states). This can be achieved by regarding the cavity photon mode as the primary bath mode with the "coordinate" \hat{q}_c that directly couples to the reaction coordinate \hat{R} , and cavity loss as the secondary bath that couples to \hat{q}_c . This multi-layer bath model has been extensively discussed in the literature, including the seminal work from Garg³⁸, as well as many others. ^{39–43} By performing a harmonic analysis of the equations of motion⁴⁴ it is shown that the model Hamiltonian of Eq. 8 has a one-to-one map (through a normal mode transformation) to the effective Hamiltonian as below, ^{38,39}

$$\hat{H} = \frac{\hat{P}^2}{2M} + V(\hat{R}) + \hat{H}_{\nu} + \hat{H}_{\text{eff}}, \tag{9}$$

where H_{ν} and its spectral density function is already defined in Eq. 4 and 6a, respectively. The cavity and its associated loss are combined as

$$\hat{H}_{\text{eff}} = \frac{1}{2} \sum_{j} \left[\hat{\hat{P}}_{j}^{2} + \tilde{\Omega}_{j}^{2} \left(\hat{\tilde{X}}_{j} - \frac{\tilde{C}_{j}}{\tilde{\Omega}_{j}^{2}} \hat{R} \right)^{2} \right], \quad (10)$$

with the effective spectral density function as below, ^{39,43}

$$J_{\text{eff}}(\omega) \equiv \frac{\pi}{2} \sum_{j} \frac{\tilde{C}_{j}^{2}}{\tilde{\Omega}_{j}} \delta(\omega - \tilde{\Omega}_{j})$$

$$= \frac{2\eta_{c}^{2} \omega_{c}^{3} J_{c}(\omega)}{\left[\omega_{c}^{2} - \omega^{2} + \tilde{R}(\omega)\right]^{2} + \left[J_{c}(\omega)\right]^{2}},$$
(11)

where $\tilde{R}(\omega)$ is expressed as

$$\tilde{R}(\omega) = \frac{2\omega^2}{\pi} \mathcal{P} \int_0^\infty ds \, \frac{J_c(s)}{s(\omega^2 - s^2)},\tag{12}$$

where \mathcal{P} in the above expression denotes principal value integral, $J_{\rm c}(\omega)$ in Eq. 11 is defined in Eq. 6b. Details of the derivations for Eqs. 9-12 are provided in Appendix C. If the secondary bath spectral density function (the photon-loss bath) takes the Drude-Lorentz form

$$J_{\rm c}(\omega) = \frac{2\lambda_{\rm c}\gamma_{\rm c}\omega_{\rm c}}{\omega^2 + \gamma_{\rm c}^2},\tag{13}$$

where $\gamma_{\rm c}$ is the bath characteristic frequency and $\lambda_{\rm c}$ is the reorganization energy, then the integral in Eq. 12 can be analytically evaluated as $\tilde{R}(\omega) = \omega J_{\rm c}(\omega)/\gamma_{\rm c}$, which is later used in our numerical evaluation. The Markovian limit will be reached when $\gamma_{\rm c} \to \infty$, hence $\tilde{R}(\omega) \to 0$, and the effective spectral density has a Brownian oscillator form³⁸

$$J_{\text{eff}}(\omega) = \frac{2\alpha \eta_{\text{c}}^2 \omega_{\text{c}}^3 \omega}{(\omega_{\text{c}}^2 - \omega^2)^2 + \alpha^2 \omega^2},\tag{14}$$

where the broadening parameter

$$\alpha \equiv 2\lambda_{\rm c}/\gamma_{\rm c} \tag{15}$$

controls the width of the spectral density. A similar argument for the Markovian limit can also be made for the Ohmic spectral density. 45 Eq. 14 is a seminal result from the early work of Leggett 44 and Garg, et al. 38 , which was derived from performing a normal-mode transformation of the bath while assuming the Markovian limit for the secondary bath. It can also be reached from the more general results in Eq. 11 by directly taking the Markovian limit. 39,43

The reorganization energy for the effective bath described by $J_{\text{eff}}(\omega)$ in Eq. 11 is given as⁴⁶

$$\lambda_{\text{eff}} \equiv \sum_{j} \frac{\tilde{C}_{j}^{2}}{2\tilde{\Omega}_{j}^{2}} = \frac{1}{\pi} \int_{0}^{+\infty} d\omega \, \frac{J_{\text{eff}}(\omega)}{\omega}. \tag{16}$$

Note that Eq. 9 corresponds to a much simpler systembath model, with linear coupling between the system and the two baths (cf. Eq. 9),

$$\hat{H} = \hat{H}_{S} + \hat{H}_{ren} + \hat{h}_{B}^{eff} + \hat{H}_{SB},$$
 (17)

where each term of the Hamiltonian is defined as

$$\hat{H}_{\rm S} = \frac{\hat{P}^2}{2M} + V(\hat{R}),$$
 (18a)

$$\hat{H}_{\rm ren} = (\lambda_{\nu} + \lambda_{\rm eff})\hat{R}^2,\tag{18b}$$

$$\hat{h}_{\rm B}^{\rm eff} = \frac{1}{2} \sum_{i} \left(\hat{p}_{i}^{2} + \omega_{i}^{2} \hat{x}_{i}^{2} \right) + \frac{1}{2} \sum_{j} \left(\hat{P}_{j}^{2} + \tilde{\Omega}_{j}^{2} \hat{X}_{j}^{2} \right), \quad (18c)$$

$$\hat{H}_{SB} = \hat{R} \otimes (\hat{F}_{\nu} + \hat{F}_{eff}), \tag{18d}$$

where \hat{H}_{ren} denotes the reorganization energy term, and the stochastic force operators are

$$\hat{F}_{\nu} \equiv \sum_{i} c_{i} \hat{x}_{i}; \quad \hat{F}_{\text{eff}} \equiv \sum_{j} \tilde{C}_{j} \hat{X}_{j}.$$
 (19)

Note that under the vibrational eigenbasis $\{|\nu_i\rangle\}$ (see Eq. 22), the $\hat{H}_{\rm ren}$ operator will be a constant matrix because it is only a function of \hat{R} . As a consequence of the above system-bath partition, the system keeps its dimension the same as the bare matter part, which has greatly reduced computational cost compared to the conventional treatment. Moreover, no truncation approximation for photon Fock states is explicitly made, and the full Hilbert space of the cavity subsystem is taken into account.

C. Model Systems

To model how VSC influences chemical reactions, we use the ground-state proton transfer model. In particular, we are interested in the one-dimensional double-well (DW) potential, 47,48

$$V(\hat{R}) = -\frac{M\omega_{\rm b}^2}{2}\hat{R}^2 + \frac{M^2\omega_{\rm b}^4}{16E_{\rm b}}\hat{R}^4,\tag{20}$$

where M is the proton mass, $\omega_{\rm b}$ is the barrier frequency given as

$$\omega_{\rm b} \equiv \sqrt{-\frac{1}{M} \cdot \frac{d^2 V}{dR^2}\Big|_{R_{\ddagger}}},\tag{21}$$

and $E_{\rm b}$ is the barrier height of the DW potential. Note that Eq. 20 assumes a symmetric DW potential. Here, we use the parameters $E_{\rm b}=2120~{\rm cm}^{-1}$ and $\omega_{\rm b}=1000~{\rm cm}^{-1}$.

For this system Hamiltonian (from Eq. 18a), the corresponding eigenvectors $|\nu_i\rangle$ and eigenenergies E_i are obtained by numerically solving

$$\hat{H}_{\rm S}|\nu_i\rangle = \left(\frac{\hat{P}^2}{2M} + V(\hat{R})\right)|\nu_i\rangle = E_i|\nu_i\rangle,$$
 (22)

where $V(\hat{R})$ is expressed in Eq. 20. These vibrational eigenstates are obtained using the discrete variable representation (DVR) basis⁴⁹ with 1001 grid points in the range of $-2.0 \le R \le 2.0$. In the quantum dynamics simulations using HEOM, we treat the number of vibrational eigenstates as a convergence parameter, and we have included a total of 10 states (from $|\nu_0\rangle$ to $|\nu_9\rangle$). Details (including the numerical convergence testing results) are provided in Sec. III of the Supplementary Material.

To facilitate the rate constant calculation, we *diabatize* the two lowest eigenstates as

$$|\nu_{\rm L}\rangle = \frac{1}{\sqrt{2}} (|\nu_0\rangle + |\nu_1\rangle), \quad |\nu_{\rm R}\rangle = \frac{1}{\sqrt{2}} (|\nu_0\rangle - |\nu_1\rangle), \quad (23)$$

which leads to two energetically degenerate diabatic states, denoted as $|\nu_{\rm L}\rangle$ and $|\nu_{\rm R}\rangle$ for states localized in the left and right wells, respectively, both with degenerated energies of $\mathcal{E}=(E_1+E_0)/2$ and a small tunneling splitting of $\Delta=(E_1-E_0)/2\approx 1.61~{\rm cm}^{-1}$ (where the energy difference between E_1 and E_0 is 2Δ). Similarly, for $\{|\nu_2\rangle, |\nu_3\rangle\}$, one can diabatize them and obtain the first excited diabatic vibrational states in the left and right wells as follows,

$$|\nu_{\rm L}'\rangle = \frac{1}{\sqrt{2}} (|\nu_2\rangle + |\nu_3\rangle); \quad |\nu_{\rm R}'\rangle = \frac{1}{\sqrt{2}} (|\nu_2\rangle - |\nu_3\rangle), \quad (24)$$

with the degenerate diabatic energy of $\mathcal{E}' = (E_3 + E_2)/2$ and the tunneling splitting of $\Delta' = (E_3 - E_2)/2 \approx 64.05 \text{ cm}^{-1}$. Note that because $|\nu_2\rangle$ and $|\nu_3\rangle$ are very close to the top of the barrier, the diabatic states $|\nu_L'\rangle$ and $|\nu_R'\rangle$ are not as well localized as $|\nu_L\rangle$ and $|\nu_R\rangle$. Based on the two diabatic states $|\nu_L\rangle$ and $|\nu_L'\rangle$ in the left well, we define the quantum vibration frequency of the reactant as

$$\omega_0 \equiv \mathcal{E}' - \mathcal{E} = 1172.2 \text{ cm}^{-1}, \tag{25}$$

which is directly related to the quantum transition of $|\nu_{\rm L}\rangle \rightarrow |\nu'_{\rm L}\rangle$. Note that the spectroscopy measurement (IR or transmission spectra) is also directly related to this frequency.

On the other hand, the classical bottom of the well frequency is directly related to the curvature of the potential as follows,

$$\omega_0^{\text{cl}} \equiv \sqrt{\frac{1}{M} \cdot \frac{d^2 V}{dR^2} \Big|_{R_0}} = \sqrt{2}\omega_{\text{b}} = 1414 \text{ cm}^{-1},$$
 (26)

where R_0 is the bottom of the well position of V(R). Note that the top of the barrier frequency, $\omega_{\rm b} = 1000~{\rm cm}^{-1}$, the classical bottom of the well frequency, $\omega_0^{\rm cl} = 1414~{\rm cm}^{-1}$, and the quantum vibration frequency, $\omega_0 = 1172.2~{\rm cm}^{-1}$, are different. Later in quantum dynamics simulations, we find that the cavity-promoted reaction rate constant is directly related to ω_0 , and the resonance effect is very sharp in frequency space, such that we are sure it is different from both $\omega_0^{\rm cl}$ and $\omega_{\rm b}$.

Further, the reaction coordinate \hat{R} is coupled to a harmonic phonon bath to model the effect of the other vibrational DOFs, where the system-bath coupling is characterized with a spectral density taken in the Drude-Lorentz form,

$$J_{\nu}(\omega) = \frac{2\lambda_{\nu}\gamma_{\nu}\omega}{\omega^2 + \gamma_{\nu}^2},\tag{27}$$

where $\gamma_{\nu} = 200 \text{ cm}^{-1}$ is the bath characteristic frequency, and λ_{ν} is the reorganization energy. We further introduce the quantity $\eta_{\nu} \equiv 2\lambda_{\nu}/(M\gamma_{\nu}\omega_b)$ to characterize the bath friction strength.⁴⁸ For the results presented in the main text, we use $\eta_{\nu} = 0.1$, which corresponds to

the Kramers under-damped regime (or energy diffusion-limited regime) for the model molecular system we considered here. Detailed discussions can be found in Sec. VI of the Supplementary Material.

The absorption spectra of the bare-molecule system outside the cavity can be described by the Lorentzian line shape, ⁵⁰

$$\mathcal{A}_{\nu}(\omega) = \frac{1}{\pi} \frac{\Gamma_{\nu}}{(\omega - \omega_0)^2 + \Gamma_{\nu}^2},\tag{28}$$

where Γ_{ν} is the line width, ω_0 is the peak position (the same as Eq. 25). The infrared (IR) spectra of the baremolecule system are numerically calculated by HEOM, in which $\Gamma_{\nu} \approx 30 \text{ cm}^{-1}$ (see Fig. 3d). Details on the calculation of IR spectra using HEOM are presented in Sec. I-D of the Supplementary Material. In recent studies of VSC rate enhancement, the bare molecular absorption has a line width of $25 \sim 30 \text{ cm}^{-1}$ (see Fig. 3c of Ref. 4 or Fig. 4 of Ref. 5). Note that this line width includes both homogeneous (captured by $J_{\nu}(\omega)$ and inhomogeneous broadenings (static disorder, not modeled here). As such, the choice of the parameter for $J_{\nu}(\omega)$ is in line with what was observed in experiments, even though the phonon bath friction η_{ν} for the molecule is in the energy diffusionlimited regime. We must emphasize that it is currently unknown in which regime VSC reactions⁷ operate. It could be either the spatial or energy diffusion-limited regime or some intermediate regime. Chemical reactions in the liquid phase are typically expected to take place in the spatial diffusion-limited regime (with strong solvent friction, also known as the plateau regime or the Kramers overdamped regime), whereas those in the gas phase are expected to take place in the energy diffusionlimited regime (with weak solvent friction, also known as the Kramers underdamped regime). However, the energy diffusion-limited regime is more prevalent than is commonly assumed²³ for chemical kinetics in liquid solvents $^{51-54}$. It is also possible for chemical reactions to be energy diffusion-limited even if the solvent friction is large, as long as the bath DOFs are slow. 20,55 To answer this question, one can perform a direct molecular dynamics simulation to extract the solvent spectral density.⁵⁶

Because all VSC experiments use a cavity that has a finite lifetime τ_c , we need to briefly discuss the connection between the cavity loss rate Γ_c and the photon bath spectral density $J_c(\omega)$. We assume $J_c(\omega)$ to be the Drude-Lorentz form as follows (cf. Eq. 13)

$$J_{\rm c}(\omega) = \frac{2\lambda_{\rm c}\gamma_{\rm c}\omega}{\omega^2 + \gamma_{\rm c}^2}.$$

Under the Markovian limit ($\gamma_c \to \infty$), the absorption line shape of the cavity mode⁵⁷ is (cf. Eq. 14-15)

$$\mathcal{A}_{\rm c}(\omega) \propto \frac{\alpha \omega}{(\omega_{\rm c}^2 - \omega^2)^2 + \alpha^2 \omega^2}.$$
 (29)

Experimentally, one can directly read the full width at half maximum (FWHM) of the optical spectra Γ_c . Here,

based on Eq. 29, the FWHM is

$$\Gamma_{\rm c} = \alpha = 2\lambda_{\rm c}/\gamma_{\rm c}.$$
 (30)

More generally, for the non-Markovian case, one can derive the loss rate Γ_c as²⁵

$$\Gamma_{\rm c} = \frac{J_{\rm c}(\omega_{\rm c})}{\omega_{\rm c}(1 - e^{-\beta\omega_{\rm c}})},\tag{31}$$

where $\beta \equiv 1/(k_{\rm B}T)$ is the inverse temperature, $k_{\rm B}$ is the Boltzmann constant. Eq. 31 will reduce to the Markovian limit (Eq. 30) when $\gamma_{\rm c} \to \infty$ and $\beta \omega_{\rm c} \gg 1$. A simple derivation of Eq. 31 is provided in Appendix D.

The cavity lifetime $\tau_{\rm c}$ and the cavity quality factor Q are related to the cavity loss rate $\Gamma_{\rm c}$ as follows,

$$\tau_{\rm c} = \frac{1}{\Gamma_{\rm c}}; \quad Q = \frac{\omega_{\rm c}}{\Gamma_{\rm c}} = \omega_{\rm c} \tau_{\rm c}.$$
(32)

For the recent VSC experiment by Ebbesen $et~al.^6$, the typical values for these parameters are $\tau_{\rm c}\approx 100$ fs and $\Gamma_c\approx 53~{\rm cm}^{-1}$. If the cavity frequency is $\omega_{\rm c}=\omega_0=1172.2~{\rm cm}^{-1}$, then the quality factor is $Q\approx 22.1$. For a different VSC experiment by Xiong,⁵⁸ the cavity lifetime was $\tau_{\rm c}\approx 1\sim 5$ ps, translating to a quality factor of $Q\approx 221\sim 1105$ for $\omega_{\rm c}=1172.2~{\rm cm}^{-1}$. In our numerical simulations, we first fix $\tau_{\rm c}$ (or equivalently, $\Gamma_{\rm c}=1/\tau_{\rm c}$), then determine $\lambda_{\rm c}$ using Eq. 31 with specified $\gamma_{\rm c}$.

Fig. 1 provides a schematic illustration of the ground state chemical reaction model and the environmental spectral density functions outside and inside the cavity. respectively. Fig. 1a presents the first few vibrational states of the DW model, denoted as $|\nu_L\rangle$, $|\nu_R\rangle$, $|\nu_L'\rangle$, $|\nu_{\rm R}'\rangle$, $|\nu_4\rangle$, and $|\nu_5\rangle$. The red arrows indicate the potential effect of the cavity modifying vibrational state transitions, and the blue arrow right above the barrier denotes the fast dissipative tunneling process from $|\nu_{\rm L}'\rangle$ to $|\nu_{\rm R}'\rangle$. Fig. 1b shows the molecular phonon bath spectral density $J_{\nu}(\omega)$ (dark blue) and the effective spectral density $J_{\text{eff}}(\omega)$ (red), which has the Brownian oscillator spectral density (Eq. 14). Later through the quantum dynamics simulations, we find that the spectral density, $J_{\rm eff}(\omega)$, can accelerate the state-to-state quantum transitions $|\nu_L\rangle \to |\nu_L'\rangle$ and $|\nu_R\rangle \to |\nu_R'\rangle$ (as indicated by the red arrows in Fig. 1a) when its peak frequency is in resonance with the quantum vibration frequency ω_0 , causing resonance enhancement effects. Detailed discussions can be found in the results of Fig. 2 and Fig. 3.

D. Quantum Dynamics Simulations of the rate constant

In this work, we use the numerically exact hierarchical equations of motion (HEOM) approach $^{59-62}$ to propagate the quantum dynamics of this VSC model. For a practical calculation, truncation has to be made upon the number of matter states, restricting the dynamics in a relatively low-energy subspace while ensuring numerical

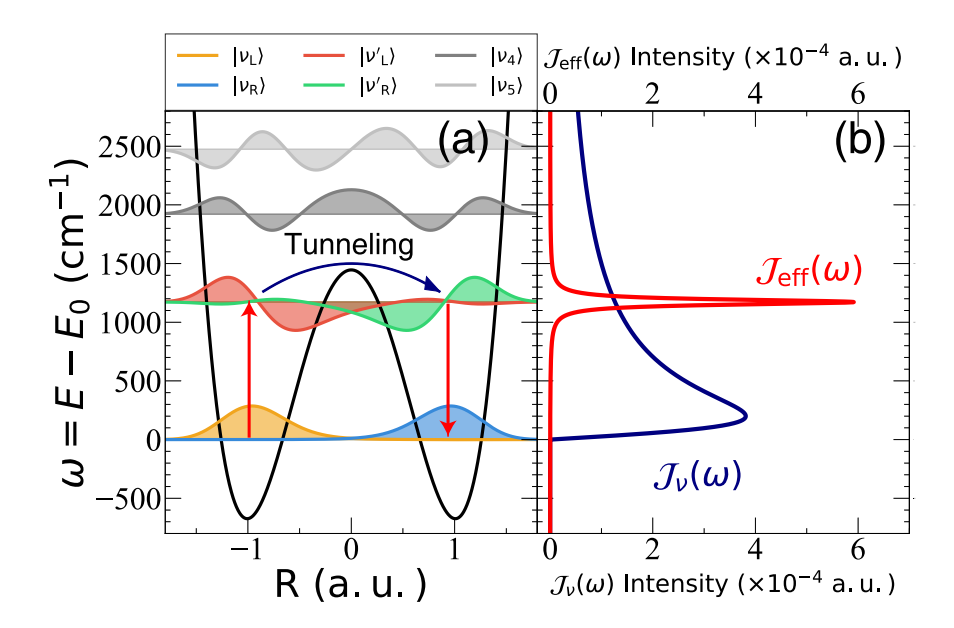


FIG. 1. Schematic illustration of the ground state chemical reaction model and the environmental spectral density functions. (a) Potential energy surface for the DW model used in this work, with the plot of the first few states. The red arrows account for cavity modification effects. The ground state population of the left well state $|\nu_{\rm L}\rangle$ are pumped to the $|\nu'_{\rm L}\rangle$ state, then transit to $|\nu'_{\rm R}\rangle$ via the tunneling splitting Δ' , and are deexcited to the right well $|\nu_{\rm R}\rangle$. (b) Plot of the molecular phonon bath spectral density function $J_{\nu}(\omega)$ (dark blue curve), plus the effective spectral density $J_{\rm eff}(\omega)$ (red curve), which corresponds to the cavity and its associated loss. Parameters are taken as $\eta_{\rm c}=0.05$, $\omega_{\rm c}=1172~{\rm cm}^{-1}$ (in resonance), and $\tau_{\rm c}=100$ fs. The corresponding rate for this $\tau_{\rm c}$ will be presented in Fig. 4 (violet curve).

accuracy. Here, we use the lowest $\mathcal{F} = 10$ vibrational eigenstates to construct the matter Hilbert subspace (see Sec. IIC.) For the model Hamiltonian in Eq. 18, the quantum subsystem is considered as $\hat{H}_{S} + \hat{H}_{ren}$, projected in the Hilbert subspace spanned by $\{|\nu_0\rangle,...|\nu_9\rangle\}$ (vibrational eigenstates of $\hat{H}_{\rm S}$), whereas $\hat{h}_{\rm B}^{\rm eff}$ is treated as bath DOFs and propagated implicitly based on the HEOM formalism. The theoretical details of the HEOM approach we used in this work are provided in Sec. I-A of the Supplementary Material. For HEOM propagation, there are several convergence control parameters, including (1) the number of bath terms obtained from the decomposition of the bare environment time-correlation function (TCF), (2) the time step for integration, (3) the depth of the EOMs (or the number of tiers), and (4) on-the-fly filtering⁶³ error tolerance. We have carefully checked all of the above convergence parameters. More specifically, we use the fourth order Runge-Kutta (RK-4) integrator with a time step of 0.025 fs, together with the on-the-fly filtering algorithm⁶³ with an error tolerance of 1×10^{-7} . More details about the bath TCF decomposition schemes and numerical calculations using HEOM are provided in Sec. I-B and I-C of the Supplementary Material.

The HEOM method requires a factorizable initial condition between the system and the bath subspaces. Note that the choice of a particular initial condition will not influence the rate dynamics or rate constant.^{48,64} We thus

assume a factorizable initial full density matrix as

$$\hat{\rho}(0) = |\nu_{\rm L}\rangle\langle\nu_{\rm L}| \otimes \frac{e^{-\beta\hat{h}_{\rm B}^{\rm eff}}}{Z_{\rm B}},\tag{33}$$

where $Z_{\rm B} \equiv {\rm Tr}_{\rm B}[e^{-\beta \hat{h}_{\rm B}^{\rm eff}}]$ is the bath partition function. which is convenient to construct since the reduced system part is a pure state.⁶⁵ We adopt the initial condition of Eq. 33 in all of our numerical simulations with HEOM. The reduced density matrix of the system, on the other hand, is defined as

$$\hat{\rho}_{S}(t) = \text{Tr}_{B}[\hat{\rho}(t)] = \text{Tr}_{x}\text{Tr}_{\tilde{X}}[\hat{\rho}(t)],$$
 (34)

where $\hat{\rho}(t)$ is the full density matrix of the system, and the trace Tr_x and $\operatorname{Tr}_{\tilde{X}}$ are performed on the phonon bath $\{x_j\}$ and the effective photon bath $\{\tilde{X}_j\}$, respectively (see Eq. 18).

In order to evaluate the forward rate constant, we follow the previous work^{25,48,66} by defining the time-dependent reactant (\mathcal{R}) and product state (\mathcal{P}) populations as

$$P_{\mathcal{R}}(t) = \text{Tr}_{\mathcal{S}}\left[(1 - \hat{h})\hat{\rho}_{\mathcal{S}}(t) \right],$$
 (35a)

$$P_{\mathcal{P}}(t) = 1 - P_{\mathcal{R}}(t), \tag{35b}$$

where the trace Tr_{S} in Eq. 35a is performed along the system DOF (which is the reaction coordinate R for the model considered here). In Eq. 35, $\hat{h} = h(\hat{R} - R^{\ddagger})$ is the Heaviside operator that projects onto the product

states, where h(R) = 1 for $R > R^{\ddagger}$ (in the product region) and h(R) = 0 for $R < R^{\ddagger}$ (in the reaction region), R^{\ddagger} is the dividing surface. For the symmetric DW model considered here, we use $R^{\ddagger} = 0$. Under the system's eigen-representation $\{|\nu_i\rangle\}$ in the truncated \mathcal{F} -dimensional Hilbert subspace, it can be evaluated as

$$P_{\mathcal{R}}(t) = \sum_{j=1}^{\mathcal{F}} \langle \nu_j | (1 - \hat{h}) \hat{\rho}_{\mathcal{S}}(t) | \nu_j \rangle$$

$$= \sum_{i,j=1}^{\mathcal{F}} \langle \nu_j | (1 - \hat{h}) | \nu_i \rangle \cdot [\hat{\rho}_{\mathcal{S}}]_{ij}(t),$$
(36)

where $[\hat{\rho}_{S}]_{ij}(t) = \langle \nu_{i} | \hat{\rho}_{S}(t) | \nu_{j} \rangle$ is the system reduced density matrix element, and $\langle \nu_{i} | (1 - \hat{h}) | \nu_{i} \rangle$ is evaluated as

$$\langle \nu_j | (1 - \hat{h}) | \nu_i \rangle = \int_{-\infty}^{+\infty} dR \ \psi_j^*(R) [1 - h(R - R^{\ddagger})] \psi_i(R)$$
$$= \int_{-\infty}^{R^{\ddagger}} dR \ \psi_j^*(R) \psi_i(R),$$

where $\psi_i(R) = \langle R | \nu_i \rangle$, $\psi_j^*(R) = \langle \nu_j | R \rangle$ are the eigenfunctions of the vibrational eigenstates in the position representation (obtained using DVR grid-based method).

The forward rate constant is then evaluated $via^{43,48,66,67}$

$$k = -\lim_{t \to t_{\rm p}} \frac{\dot{P}_{\mathcal{R}}(t)}{P_{\mathcal{R}}(t) + \chi_{\rm eq} \cdot [P_{\mathcal{R}}(t) - 1]},\tag{37}$$

where $\chi_{\rm eq} \equiv \langle P_{\mathcal{R}} \rangle / \langle P_{\mathcal{P}} \rangle$ denotes the ratio of equilibrium population between the reactant and product. The time derivative $P_{\mathcal{R}}(t)$ is evaluated numerically. A simple derivation is provided in Appendix B. For the symmetric DW potential model (Eq. 20) considered in this work, $\chi_{\rm eq} = 1$, and for more general cases, it can be obtained either by path-integral Monte Carlo approaches⁶⁸ or by the imaginary time evolution of HEOM.⁶⁹ The limit $t \to t_{\rm p}$ represents that the dynamics have already entered into the rate process regime (linear response regime) and $t_{\rm p}$ represents the "plateau" time of the time-dependent rate (which is equivalent to a flux-side time correlation function formalism^{48,70,71}). A detailed discussion is provided in Appendix B. Without taking the limit $t \to t_p$, one can view Eq. 37 as the flux-side correlation function that provides the time-dependent rate constant k(t), which captures both the initial transient dynamics (the oscillatory behaviors of k(t) and the longer time rate process (plateau of k(t)). An example of this k(t) is provided in Fig. 3a. With the above preparations, we applied HEOM to solve the quantum dynamics and compute the rate constants. The bare reaction kinetics and VSC "resonance effect" under the influence of various parameters are investigated.

III. RESULTS AND DISCUSSIONS

A. Quantum Dynamics of the VSC-enhanced Reaction.

Fig. 2 presents the population dynamics of the vibrational states outside the cavity (dashed lines) and coupled to a resonant cavity for $\omega_{\rm c} = \omega_0 = 1172 \; {\rm cm}^{-1}$ (solid lines). The temperature is T = 300 K, the light-matter coupling strength is $\eta_c = 0.1$, the characteristic frequency of the photon-loss bath is $\gamma_c \to \infty$, and the cavity lifetime is set to be $\tau_c = 200$ fs (in line with the cavity used in the typical VCS experiments⁶). The initial condition is described in Eq. 33, which corresponds to a thermally activated process of the system by the environment. The populations of the six lowest vibrational states are presented, including $|\nu_{\rm L}\rangle$ (golden) in panel a, as well as $|\nu_{\rm R}\rangle$ (blue) $|\nu_{\rm L}'\rangle$ (red), $|\nu_{\rm R}'\rangle$ (green), $|\nu_4\rangle$ (dark gray), $|\nu_5\rangle$ (light gray) in panel b. Fig. 2a presents the population dynamics of $|\nu_{\rm L}\rangle$ state (the initially populated state). One can clearly see that when the resonant cavity mode ($\omega_c = \omega_0 = 1172 \text{ cm}^{-1}$) is coupled to the molecular vibrations (solid line), the population of $|\nu_{\rm L}\rangle$ decays much faster than the cavity-free case (dashed line). Fig. 2b shows the population dynamics of the other five vibrational states, with the lower panel zooms into the short-time dynamics.

We first examine the reaction mechanism for the molecule outside the cavity (dashed lines). By looking into the short-time dynamics $(t \in [0, 1.5] \text{ ps})$, as shown in the bottom panel of Fig. 2, one can clearly see the rise of the $|\nu'_{\rm L}\rangle$ population (red) during the first 1 ps, which then reaches a steady state. The rise of the $|\nu_{\rm R}'\rangle$ population (green) follows the rise of the $|\nu'_{\rm L}\rangle$ population due to its diabatic coupling with $|\nu_{\rm L}'\rangle$ through Δ' (tunneling splitting between $|\nu_2\rangle$ and $|\nu_3\rangle$) and then reaches a steady population after 1 ps. Finally, the increase in $|\nu_{\rm R}\rangle$ population (blue) follows the increase in $|\nu_{\rm R}'\rangle$ population. The high-lying excited vibrational states $|\nu_4\rangle$ and $|\nu_5\rangle$ are less populated (for both cavity-free and cavity-coupling cases), indicating a less important role in this system reaction dynamics at T = 300 K, due to their higher energy. As such, a qualitative understanding of the basic reaction mechanism for the molecule outside the cavity is $|\nu_{\rm L}\rangle \to |\nu_{\rm L}'\rangle$ due to the phonon coupling (mediated by the \hat{H}_{ν} term in Eq. 4), and then $|\nu'_{\rm L}\rangle \rightarrow |\nu'_{\rm R}\rangle$ through the vibrationally excited states tunneling splitting Δ' , and finally $|\nu_{\rm R}'\rangle \rightarrow |\nu_{\rm R}\rangle$ through vibration relaxation (again mediated by \hat{H}_{ν}).

When coupling molecular vibration to the resonant cavity (solid lines), the populations of $|\nu_{\rm R}\rangle$ (blue) increase significantly compared to the cavity-free case (dashed lines). Note that the population of $|\nu_{\rm R}\rangle$ has a steady accumulation for both inside cavity (solid) and outside cavity (dash) situations, indicating a well-defined rate process. On the other hand, this enhancement of population growth is not very significant for higher-energy vibrational states, such as $|\nu_4\rangle$ (dark gray) and $|\nu_5\rangle$ (light

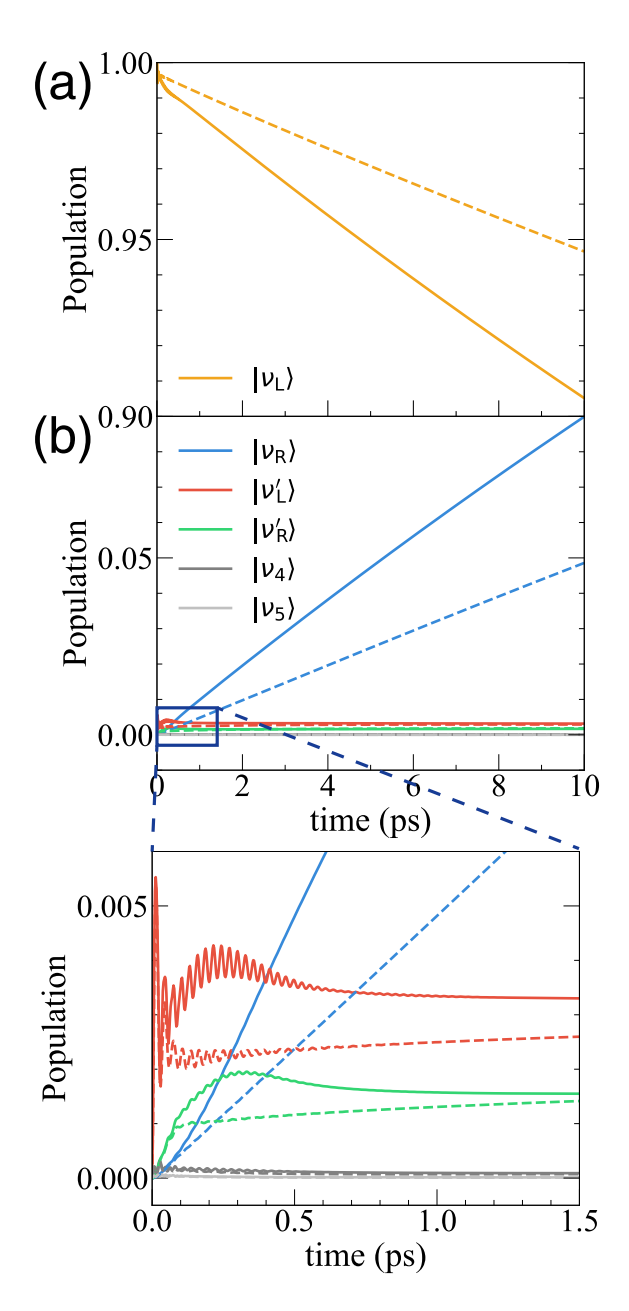


FIG. 2. Population dynamics of the lowest six states, $\{|\nu_{\rm L}\rangle, |\nu_{\rm R}\rangle, |\nu_{\rm L}'\rangle, |\nu_{\rm R}'\rangle, |\nu_{\rm 4}\rangle, |\nu_{\rm 5}\rangle\}$, inside a resonant cavity (solid lines) and outside the cavity (dash lines). The parameters are taken as $\eta_{\rm c}=0.1,\ \omega_{\rm c}=\omega_0=1172\ {\rm cm}^{-1}$ (at resonance), $\gamma_{\rm c}\to\infty$, and $\tau_{\rm c}=200\ {\rm fs.}$ (a) population dynamics of $|\nu_{\rm L}\rangle$; (b) population dynamics of $|\nu_{\rm R}\rangle$ (blue), $|\nu_{\rm 2}\rangle$ (red), $|\nu_{\rm 3}\rangle$ (green), $|\nu_{\rm 4}\rangle$ (dark gray), $|\nu_{\rm 5}\rangle$ (light gray). The short-time dynamics are highlighted in the panel below (b).

gray), indicating their less important role in the VSC process at T=300 K. When coupled to a resonant cavity (solid), the steady-state populations of $|\nu_{\rm L}'\rangle$ and $|\nu_{\rm R}'\rangle$ for the cavity-coupling case are slightly larger than the cavity-free case. In other words, the steady-state populations of those low-lying vibrational excited states are enhanced due to the presence of a cavity mode (and its

associated loss described by a photon bath), when it is in resonance with the quantum vibration frequency ω_0 .

The enhancement of the $|\nu'_{\rm L}\rangle$ population is very sensitive to the cavity frequency ω_c , which needs to match the quantum vibration frequency ω_0 (i.e., the transition frequency of $|\nu_L\rangle \rightarrow |\nu_L'\rangle$). A small deviation of ω_c away from ω_0 will cause a much less significant enhancement of the $|\nu_{\rm L}'\rangle$ population and thus the $|\nu_{\rm R}'\rangle$ or $|\nu_{\rm R}\rangle$ populations (see Fig. 3b). Furthermore, when looking at the transient behaviors of population dynamics, one finds that when $\omega_{\rm c} = \omega_0$, the $|\nu_{\rm L}'\rangle$ and $|\nu_{\rm R}'\rangle$ states have faster population gain than the cavity-free case. This is because the cavity mode promotes the $|\nu_{\rm L}\rangle \rightarrow |\nu_{\rm L}'\rangle$ transition. This mechanism for the VSC-enhanced reactions has been previously discussed in the context of "RPV mode", 48 in which it was found that an additional nuclear vibration mode can promote the proton transfer reaction rate constant. Here, our observation suggests that the cavity photon coordinate \hat{q}_c acts just like a "RPV mode". 48 The only difference is that the cavity mode \hat{q}_c has a frequency ω_c that can be easily (and continuously) tuned, whereas the frequency of RPV modes is not very easy to tune without doing chemical modifications.

B. Analytic Theory for the Resonant VSC Effect

In order to qualitatively (or even semi-quantitatively) understand the behavior of the VSC-modified rate constants, we develop an analytic theory to explain the observed dynamics. Our starting point is based on the quantum dynamics we have seen in Fig. 2. The basic kinetics can be summarized as follows,

$$|\nu_{\rm L}\rangle \xrightarrow{k_1} |\nu_{\rm L}'\rangle \xrightarrow{k_2} |\nu_{\rm R}'\rangle \xrightarrow{k_3} |\nu_{\rm R}\rangle,$$
 (38)

where k_1 and k_3 are dominated by the phonon or photonmediated population transfer, and k_2 is dominated by excited state tunneling splitting Δ' . Here, we explicitly ignored other high-lying vibrational states $|\nu_4\rangle$ and $|\nu_5\rangle$ due to their negligible population (see Fig. 2), as well as the vibrational ground state tunneling pathway $|\nu_L\rangle \rightarrow |\nu_R\rangle$ due to the small tunneling splitting Δ . Based on the observation of the population dynamics in Fig. 2, it seems that both populations of $|\nu'_L\rangle$ and $|\nu'_R\rangle$ reach steady states. As such, the dynamics of our model systems (both inside and outside the cavity) are classic textbook examples of steady-state kinetics. This means that the product population under the steady-state limit can be approximated as (see details in Appendix B)

$$[\nu_{\rm R}(t)] = [\nu_{\rm L}(0)] \cdot (1 - e^{-k_1 t}),$$
 (39)

where $[\nu_{\rm R}](t)$ denotes the time-dependent population of the product well state $|\nu_{\rm R}\rangle$ under the steady-state approximation, and $[\nu_{\rm L}(0)]$ denotes the initial population of $|\nu_{\rm L}\rangle$. Eq. 39 indicates that under the steady-state limit, the reaction rate constant is described by the growth of the $|\nu_{\rm R}\rangle$ population, with the apparent rate constant k_1 . As such, under the steady-state approximation for $|\nu_{\rm L}'\rangle$ and $|\nu_{\rm R}'\rangle$, the forward rate constant of the reaction is approximate as the rate constant of the $|\nu_{\rm L}\rangle \rightarrow |\nu_{\rm L}'\rangle$ transition, which is true for both inside the cavity and outside the cavity situations because both cases exhibit steady-state behavior for the populations of the $|\nu_{\rm L}'\rangle$ and $|\nu_{\rm R}'\rangle$ states. This means

$$k \approx k_1 = k_0 + k_{\text{VSC}}.\tag{40}$$

In the second equality in Eq. 40, we further decompose the rate constant into two parts, where k_0 is the outside cavity rate constant and $k_{\rm VSC}$ denotes the cavity modification part.

To analytically express the net enhancement in the rate constant for the $|\nu_{\rm L}\rangle \rightarrow |\nu'_{\rm L}\rangle$ transition, denoted as $k_{\rm VSC}$, we use Fermi's Golden Rule (FGR) with the detailed derivation provided in Appendix A. For a given $\omega_{\rm c}$, the result accounting for VSC effects on rate constant is⁵⁰

$$k_{\rm VSC} = \int_0^\infty d\omega \ \kappa(\omega) G(\omega - \omega_0),$$
 (41)

which is a convolution between $\kappa(\omega)$ and $G(\omega-\omega_0)$. Here, $\kappa(\omega)$ is the FGR rate constant for the transition $|\nu_L\rangle \rightarrow |\nu_L'\rangle$ (with a frequency ω), reading as

$$\kappa(\omega) = 2|\Delta_x|^2 \cdot J_{\text{eff}}(\omega) \cdot n(\omega), \tag{42}$$

where $\Delta_x = \langle \nu_{\rm L}' | \hat{R} | \nu_{\rm L} \rangle$ is the transition dipole matrix element, and $n(\omega) = 1/(e^{\beta \omega} - 1)$ is the Bose-Einstein distribution function. Note that $J_{\rm eff}(\omega)$ explicitly contains $\omega_{\rm c}$, thus giving the $\omega_{\rm c}$ dependence of $k_{\rm VSC}$. Furthermore, the term $G(\omega - \omega_0)$ in Eq. 41 is an inhomogeneous broadening function for the quantum vibration frequency ω_0 , with a variance of (cf. Eq. A6)

$$\sigma^2 = \epsilon_z^2 \cdot \frac{1}{\pi} \int_0^\infty d\omega \ J_\nu(\omega) \coth(\beta \omega/2),$$

where $\epsilon_z = \langle \nu_{\rm L}' | \hat{R} | \nu_{\rm L}' \rangle - \langle \nu_{\rm L} | \hat{R} | \nu_{\rm L} \rangle$. This broadening is due to the molecular phonon bath $J_{\nu}(\omega)$.

Note that the rate expression in Eq. 41 explicitly depends on both the cavity frequency $\omega_{\rm c}$ from $J_{\rm eff}(\omega)$ in Eq. 11 and the quantum vibration frequency ω_0 from $G(\omega-\omega_0)$ in Eq. A10. In principle, one can use the convolution theorem to evaluate the expression in Eq. 41, the detailed discussions are provided in Appendix A. Unfortunately, a closed analytic formalism is not available. Instead, we numerically evaluate the expression in Eq. A21, using a spectral density discretization procedure outlined in Ref. 56. However, we find that in two special cases, analytic expressions for the approximate evaluation of $k_{\rm VSC}$ in Eq. 41 are available. For both cases, we assume the Markovian limit for the effective spectral density $J_{\rm eff}(\omega)$ (Eq. 14). Similar expressions can be derived for the non-Markovian case.

First, under the lossless limit $(\tau_c \to \infty)$, the effective spectral density function will reduce to a single δ -function, $J_{\rm eff}(\omega) \approx \pi \eta_c^2 \omega_c^2 \delta(\omega - \omega_c)$. As a result, the

broadening is fully dictated by the variance of the Gaussian,

$$k_{\rm VSC} \approx 2|\Delta_x|^2 \cdot \pi \eta_{\rm c}^2 \omega_{\rm c}^2 \int_0^\infty d\omega \ \delta(\omega - \omega_{\rm c}) G(\omega - \omega_0) n(\omega)$$
$$= 2\pi |\Delta_x|^2 \eta_{\rm c}^2 \omega_{\rm c}^2 \ G(\omega_{\rm c} - \omega_0) \cdot n(\omega_{\rm c}). \tag{43}$$

The rate profile described in Eq. 43 is a Gaussian function centered at ω_0 with respect to cavity frequency ω_c . The numerical value of these broadening factors at $T=300~\rm K$ is $^{72}~\sigma=30.83~\rm cm^{-1}$. As a comparison, $\alpha=5.3~\rm cm^{-1}$ when $\tau_c=1~\rm ps$.

Second, under the limit when the broadening caused by $J_{\nu}(\omega)$ is much smaller than the one caused by $J_{\rm eff}(\omega)$, which means that $\alpha \gg \sigma$ (for example, when $\tau_{\rm c} \to 0$ or $\alpha \to \infty$), the Gaussian function is much narrower than $J_{\rm eff}(\omega)$, such that we can approximate $G(\omega - \omega_0)$ as a single δ -function, $G(\omega - \omega_0) \approx \delta(\omega - \omega_0)$. Then the $k_{\rm VSC}$ expression in Eq. 41 becomes

$$k_{\text{VSC}} \approx \kappa(\omega_0) = 2|\Delta_x|^2 \cdot J_{\text{eff}}(\omega_0) \cdot n(\omega_0), \qquad (44)$$
$$\approx 2|\Delta_x|^2 \cdot \frac{2\alpha\eta_c^2\omega_0^3\omega_0}{(\omega_c^2 - \omega_0^2)^2 + \alpha^2\omega_0^2} \cdot e^{-\beta\omega_0},$$

such that the cavity-related width $\alpha = \tau_{\rm c}^{-1}$ (see Eq. 30) dominates the rate profile. For the model parameter considered here ($\omega_0 = 1172 \text{ cm}^{-1}$, $k_{\rm B}T \approx 200 \text{ cm}^{-1}$), we have $\beta\omega_0 \gg 1$ and thus $n(\omega_0) \approx e^{-\beta\omega_0}$, as we explicitly used in the second line of Eq. 44, indicating the thermal Boltzmann probability of occupying the $|\nu_1'\rangle$ state. For larger τ_c , it is necessary to use the full FGR expression in Eq. 41 (with convolution), while the approximate expression in Eq. 44 provides a much simpler analytic form for us to analyze basic scaling relations of k_{VSC} . In particular, the resonant behavior can be readily seen because $k_{\rm VSC}$ will reach its maximum when $\omega_{\rm c}=\omega_0$. The broadening of the VSC-modified rate profile in Eq. 44 is dictated by the parameter α (see the expression in Eq. 15), which is the width of $J_{\text{eff}}(\omega)$ in Eq. 14. Further, when α is much larger than ω_c , the Brownian lineshape will gradually become the familiar Drude-Lorentz lineshape.³⁹ The more general expression in Eq. 41 will predict the same resonant condition if $J_{\text{eff}}(\omega)$ takes the Markovian limit (Eq. 14), because the function $G(\omega - \omega_0)$ in Eq. A10 only provides additional broadening.

The VSC-modified rate constant $k_{\rm VSC}$, expressed in Eq. 41 and its approximate versions in Eq. 43 and Eq. 44, are the **key theoretical results** of this work. The approximate expression in Eq. 44, although less accurate, readily provides an intuitive understanding of the VSC modifications on the rate constant. Under the limit of $J_{\rm eff}(\omega_0) \rightarrow 0$, $k_{\rm VSC} \rightarrow 0$, the effect of the cavity will diminish, and the rate constant (Eq. 40) will be reduced back to the situation of the outside cavity. This limit can be achieved by three possible scenarios: (1) the lightmatter coupling strength $\eta_c \rightarrow 0$ (a trivial limit). (2) for non-negligible η_c , one still has $J_{\rm eff}(\omega_0) \rightarrow 0$ if there is a large frequency difference between ω_c and ω_0 (see

Eq. 14). (3) when $\alpha \to \infty$, or the cavity lifetime $\tau_c \to 0$ (see Eq. 32), meaning either $\lambda_c \to \infty$ and/or $\gamma_c \to 0$, both of which correspond to an extremely lossy cavity. We will revisit this simple rate expression when further analyzing the numerical results of the VSC-modified rate constant in the following sections.

Finally, before moving on to the numerical results, we want to comment on the isotropic disorder of the dipole relative to the field polarization direction. It is believed that the dipole orientation inside the cavity should have been isotropically disordered, such that

$$\chi \cdot \mu(\hat{R}) = \chi \cdot \hat{\mu} \cos \varphi, \tag{45}$$

where φ is the angle between the dipole operator $\hat{\mu}$ and the field polarization direction \hat{e} , which has a uniform distribution in $[0, 2\pi)$. One can replace the definition of η_c in Eq. 7 as follows

$$\eta_{\rm c} = \sqrt{\frac{1}{2\epsilon_0 \omega_{\rm c} \mathcal{V}}} \cos \varphi. \tag{46}$$

We expect that the rotation of the dipole will be much slower than that of the dynamics processes, which can be treated as a static disorder and averaged out. Because all of the FGR expressions depend on $\eta_{\rm c}$ quadratically inside $J_{\rm eff}(\omega)$, the factor $\cos\varphi$ will show up. Upon statistical averaging, the FGR rate in Eq. 41 will be modified as

$$k_{\rm VSC} = \langle \cos^2 \varphi \rangle \cdot \int_0^\infty d\omega \ \kappa(\omega) G(\omega - \omega_0),$$
 (47)

where $\langle \cos^2 \varphi \rangle = 1/3$ for fully isotropic case. As a result, all of the approximate FGR rate expressions, including Eq. 43 and Eq. 44, will be modified by multiplying a factor of $\langle \cos^2 \varphi \rangle = 1/3$. Note that this is a unique feature of the quantum FGR theory, in which the η_c^2 feature is the key to surviving the isotropic averaging. Previous classical GH theory²² will not survive isotropic averaging and will give zero modification of the rate constant.

C. VSC Rate Modifications by changing ω_c and η_c

Fig. 3 presents the VSC-modified rate profile as a function of the cavity frequency ω_c . Here, the light-matter coupling strength η_c and the cavity frequency ω_c are variables. The temperature is set to be T = 300 K, the characteristic frequency of the photon-loss bath is $\gamma_{\rm c} \to \infty$, and the cavity lifetime is chosen to be $\tau_{\rm c} = 100$ fs. Fig. 3a presents the time-dependent rate constant k(t) (see discussions below Eq. 37) inside a resonant cavity (with $\omega_c = \omega_0 = 1172 \text{ cm}^{-1}$). As one gradually increases the light-matter coupling strength η_c (see legend in panel a) from 0 (black, outside the cavity) to 0.0125 (violet), 0.01875 (blue), 0.025 (cyan), 0.0375 (green), 0.05 (orange), 0.075 (red) and 0.1 (brown), there is always a well-defined plateau value that provides a rate constant (associated with a rate process), with the plateau time $t_{\rm p} \approx 2 \text{ ps.}$

Fig. 3b presents the resonance effect of the VSCmodified rate constant when a molecular vibration is coupled to a cavity. A resonantly enhanced sharp peak of the rate constant is exhibited when $\omega_{\rm c} = \omega_0$. To characterize cavity modification effects, we present the rate constant enhancement factor k/k_0 from Fig. 3a, after reaching the dynamic plateau time. As η_c increases, the resonance peak intensity also becomes stronger. This sharp resonance enhancement of the rate constant has been observed in recent VSC experiments, such as Fig. 3d of Ref. 4 or Fig. 4 of Ref. 5. However, we need to remind the reader that in experiments^{4,5} there are at least 10⁶ molecules collectively coupled to the cavity, whereas the current studies only considered a single molecule strongly coupled to the cavity mode. Further, in that experiment,^{4,5} the cavity mode is tuned to be resonant with solvent vibrations, while, in our model system, the cavity frequency is tuned to match the $|\nu_L\rangle \rightarrow |\nu_L'\rangle$ transition for the reactant well. Future studies will be needed that will be based on a model system that more accurately reflects the experimental setup.²² Note that because there is a clear frequency separation between the quantum transition frequency ω_0 (Eq. 25) and the classical bottom of the well frequency $\omega_0^{\rm cl}$ (all of which are labeled as the vertical dashed lines in Fig. 3b), the results clearly demonstrate that the VSC rate enhancement is only related to ω_0 (Eq. 25), rather than $\omega_0^{\rm cl}$ (Eq. 26) or $\omega_{\rm b}$ (Eq. 21). Interestingly, experimental observation always suggests that the VSC-modified rate profile and the transmission spectra of the bare molecule peaks at ω_0 (e.g., Fig. 3 of Ref. 4 and Fig. 4 of Ref. 5). This is because, in the spectra measurements, the laser field causes the transition $|\nu_{\rm L}\rangle \rightarrow |\nu_{\rm L}'\rangle$, resulting in a maximum intensity of the signal at the transition frequency ω_0 . For the VSC-modified rate profile, the cavity mode $\hat{q}_{\rm c}$ will promote the transition $|\nu_{\rm L}\rangle \rightarrow |\nu_{\rm L}'\rangle$, which reaches its highest magnitude when $\omega_c = \omega_0$. This explains why the molecular transmission spectra always show the same peak position as the VSC-modified rate profile.²⁵ This resonance structure is also predicted and explained by the FGR expression in Eq. 44, where the VSC-modified rate profile will peak at $\omega_{\rm c} = \omega_0$. The rate profile should also have a finite width around ω_0 , including both contributions from both α in $J_{\text{eff}}(\omega)$ and $G(\omega - \omega_0)$. We will return to the quantitative comparison of k_{VSC} using the full expression in Eq. 41 and the HEOM results at the end of the paper.

Fig. 3c presents the value of k/k_0 (red open circles) when $\omega_c = \omega_0$, as a function of the light-matter coupling strength η_c . The data points obtained from the exact HEOM simulations are depicted with circles, and the solid line provides a fitting curve using the first 5 data points (for the range of $\eta_c < 0.05$). The fitting suggests that k/k_0 has an almost perfect quadratic dependence to η_c for the range of $\eta_c < 0.05$, such that $k/k_0 \propto 1 + C \cdot \eta_c^2$, where $C = 4|\Delta_x|^2\omega_0\tau_c$ (see Eq. 44). This scaling relation can also be intuitively understood using the FGR expression in Eq. 41. Note that η_c in-

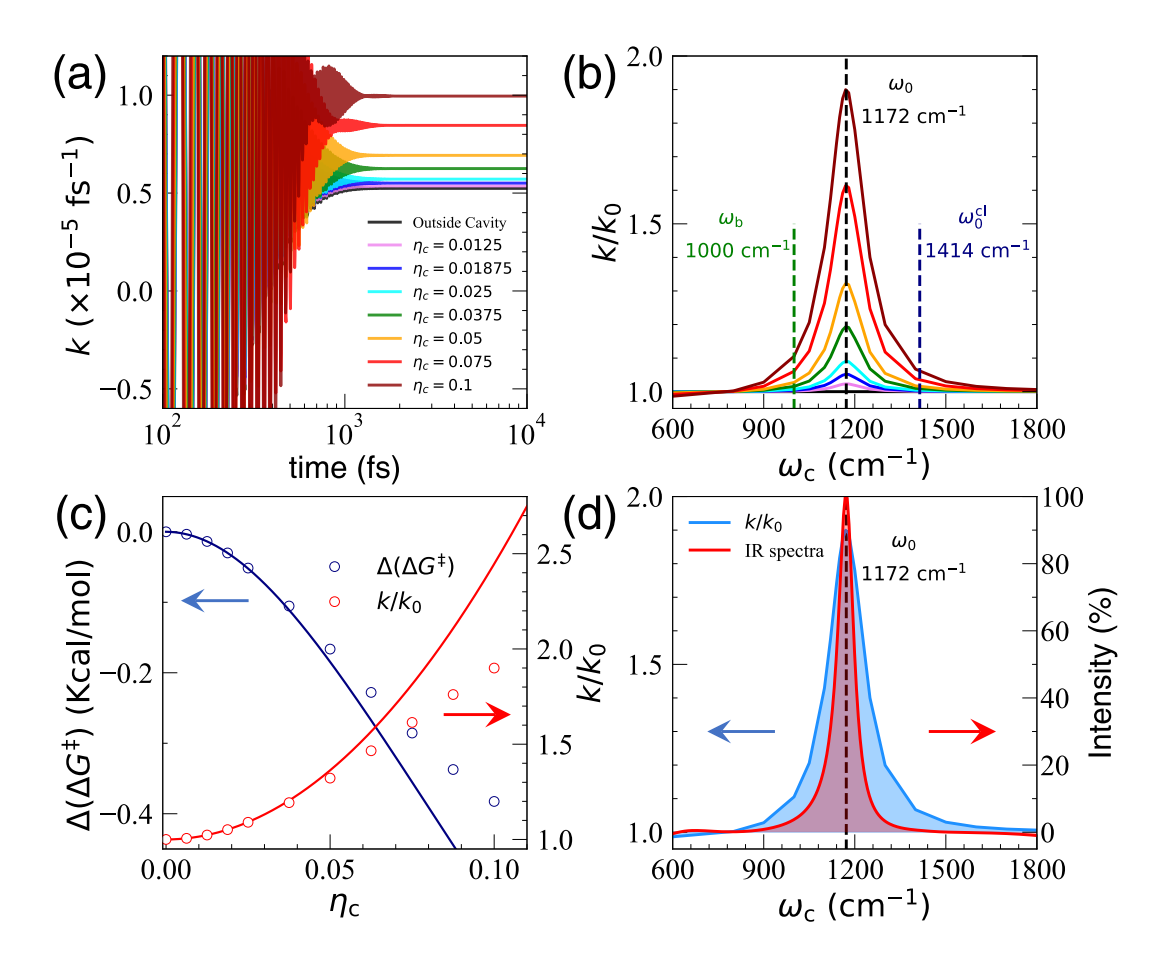


FIG. 3. Effect of the light-matter coupling strength η_c as well as cavity frequency ω_c on the forward rate constant. Fixed parameters are $\tau_c = 100$ fs and $\gamma_c \to \infty$. (a) The time-dependent rate constants k(t) (see Eq. 37 and discussions below) inside the resonant cavity ($\omega_c = \omega_0 = 1172 \text{ cm}^{-1}$). (b) Effect of η_c on the resonance peak. The FWHM of the rate profiles is around 140 cm⁻¹. (c) The rate constant enhancement factor k/k_0 (red) at resonance ($\omega_c = \omega_0 = 1172 \text{ cm}^{-1}$) versus the light-matter coupling strength η_c . The red circles are obtained from the HEOM simulations (panel b), and the red curve is a polynomial fitting using the first five data points. The change of the effective free energy barrier height $\Delta(\Delta G^{\ddagger})$ (blue circles, obtained from red circles) that backed out from k/k_0 , suggesting a scaling relation of $\Delta(\Delta G^{\ddagger}) \propto -\ln(1 + \mathcal{C} \cdot \eta_c^2)$ (blue line, obtained from red line). (d) The Rate profile (blue curve, same as the brown curve in panel b with $\eta_c = 0.1$) and IR spectra of the bare-molecule system (red curve).

fluences the intensity of the effective spectral density through $J_{\rm eff}(\omega_0) \propto \eta_{\rm c}^2$. As such, the cavity enhances the transition of $|\nu_{\rm L}\rangle \rightarrow |\nu_{\rm L}'\rangle$, hence enhancing the rate constant with a scaling relation of $\eta_{\rm c}^2$. One can also use the Rabi splitting, $\Omega_{\rm R} \equiv 2\chi\mu_{\rm LL'} = 2\eta_{\rm c}\omega_{\rm c} \cdot \mu_{\rm LL'}$ (cf. Eq. E3), to describe the rate constant. Here the transition dipole moment $\mu_{\rm LL'} = \langle \nu_{\rm L} | \mu(\hat{R}) | \nu_{\rm L}' \rangle$. See Appendix E for details. As such,

$$k/k_0 \propto 1 + \mathcal{C}' \cdot (\Omega_{\rm R}/2\omega_{\rm c})^2$$
, (48)

where $\mathcal{C}' = 4\omega_0\tau_c$. Both our numerical results and analytic analysis suggest that the VSC-enhanced reaction rate constant scales with $(\Omega_R/2\omega_c)^2$ for a relatively small light-matter coupling strength (when $\Omega_R \ll k_BT$). Although there are not many results available in the literature to confirm this trend, existing data points (such as Fig. 4b of Ref. 4) do that clearly deviate from a linear fit of $\Omega_R/2\omega_c$. However, it is difficult to conclude whether

these four experimental data points confirm a $(\Omega_R/2\omega_c)^2$ scaling. Further experimental investigations on these existing reactions⁴ will be needed to test the scaling relation between k/k_0 and Ω_R to confirm or disprove the current theoretical prediction in Eq. 48.

Fig. 3c further presents the change of the effective free energy barrier $\Delta(\Delta G^{\ddagger})$, directly calculated from the rate constant ratio k/k_0 obtained from HEOM simulations. To account for the "effective change" of the Gibbs free energy barrier $\Delta(\Delta G^{\ddagger})$, we consider the simple rate equation $k = A \cdot \exp(-\beta \Delta G^{\ddagger})$, with the outside the cavity case as $k_0 = A \cdot \exp(-\beta \Delta G^{\ddagger})$, as is commonly assumed by experimental analysis.^{3,4} The prefactor A is assumed to be the same with or without the cavity.^{3,4} The change of the effective free energy barrier compared to the bare molecular reaction (with k_0 and ΔG_0^{\ddagger}) is then

$$\Delta(\Delta G^{\ddagger}) = \Delta G^{\ddagger} - \Delta G_0^{\ddagger} = -k_{\rm B}T \ln(k/k_0). \tag{49}$$

Note that this is not an actual change in the free-energy barrier, but rather a purely kinetic effect. Based on our Eq. 48, we *predict* that

$$\Delta(\Delta G^{\ddagger}) \propto -k_{\rm B}T \ln \left[1 + \mathcal{C}' \cdot (\Omega_{\rm R}/2\omega_{\rm c})^2\right],$$
 (50)

which is also supported by the HEOM results (blue open circles). If one hypothesizes that an unknown mechanism forces the upper or lower vibrational polariton states to be a "gateway of VSC polaritonic chemical reactions" ⁷³, then the activation free energy change should shift linearly¹⁶ with $\Omega_{\rm R}$. On the other hand, the experimental results demonstrate the nonlinearity of the reaction barrier^{3,4}. Our current theory (Eq. 41) indicates that the nonlinear increase of "effective $\Delta(\Delta G^{\ddagger})$ " in Eq. 50 when increasing $\Omega_{\rm R}$ is due to the cavity promotion of the $|\nu_{\rm L}
angle
ightarrow |
u_{
m L}'
angle$ transition, and more specifically, the effective $\Delta(\Delta G^{\ddagger})$ scales with $-k_{\rm B}T \ln \left[1 + \mathcal{C}' \cdot (\Omega_{\rm R}/2\omega_{\rm c})^2\right]$. Furthermore, in Ref. 7, it was pointed out that a very small Rabi splitting observed in optical spectra can lead to much larger changes in activation free energy, such that $\Delta(\Delta G^{\ddagger}) > \Omega_{\rm R}$, which seems to be a general trend in most VSC experiments.³ But this phenomenon lacks a theoretical explanation. Here, we attempt to provide one, with $k \propto \eta_c^2$ which significantly influences the rate and, correspondingly, the effective free energy barrier.

Fig. 3d presents the rate profile (blue), which is the same as the brown curve in panel b (with $\eta_c=0.1$), as well as the IR spectra calculated by HEOM (red). Details about the IR spectral calculation using HEOM are presented in Sec. I-D of the Supplementary Material. The IR spectra have a FWHM of about 60 cm⁻¹, and a peak position of $\omega_c=\omega_0$. The VSC modified rate profile has a FWHM of 140 cm⁻¹. The same peak position strongly indicates its common origin associated with the $|\nu_L\rangle \rightarrow |\nu_L'\rangle$ transition. The optical transition is caused by $-\hat{\mu}\cdot E(t)$, where $\hat{\mu}$ is the transition dipole operator, and E(t) is the classical laser field, whereas the molecule-cavity coupling is caused by $\hat{\mu}(\hat{a}^\dagger + \hat{a}) \propto \hat{\mu} \cdot \hat{q}_c$, where $\hat{q}_c = \sqrt{1/(2\omega_c)}(\hat{a}^\dagger + \hat{a})$ is the photonic coordinate that is proportional to the displacement field intensity inside the cavity.

D. VSC Rate Modifications by changing τ_c

Fig. 4 presents the VSC-modified reaction rate constant under the influence of the cavity lifetime τ_c , with a fixed $\eta_c = 0.05$. The τ_c parameter determines the shape and intensity of the effective spectral density function $J_{\rm eff}(\omega)$. We consider the Markovian loss by setting $\gamma_c \to \infty$, which means that the effective spectral density $J_{\rm eff}(\omega)$ becomes the Brownian form in Eq. 14.

Fig. 4a presents $J_{\rm eff}(\omega)$ under different cavity lifetimes, where we fix $\omega_{\rm c} = \omega_0 = 1172~{\rm cm}^{-1}$. One can observe that $J_{\rm eff}(\omega)$ exhibits a sharp peak when there is a relatively long $\tau_{\rm c}$. It will reduce to a Dirac δ -function at the lossless limit ($\tau_{\rm c} \to \infty$), whose bare-bath TCF is discussed in Sec. I-B of the Supplementary Material. Decreasing

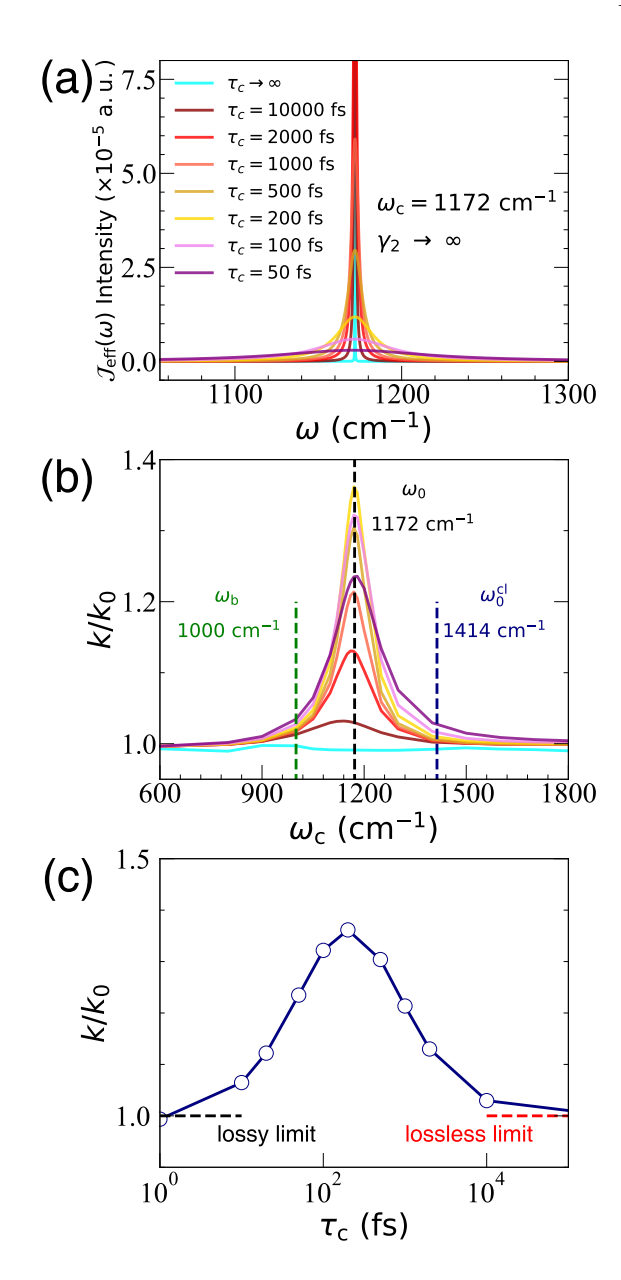


FIG. 4. Effect of cavity lifetime τ_c on the VSC-modified rate profile under the Markovian limit of the photon bath. The light-matter coupling strength is fixed as $\eta_c = 0.005$. (a) Plots of $J_{\rm eff}(\omega)$ under different τ_c , while fixing the cavity frequency $\omega_c = \omega_0 = 1172~{\rm cm}^{-1}$. (b) Effect of τ_c on the value of k/k_0 . Note that the cavity modification effects become smaller when τ_c is reduced, and the cavity effect vanishes under the heavy loss limit ($\tau_c \to 0$). (c) The peak value of k/k_0 (at $\omega_c = \omega_0$) as a function of cavity lifetime τ_c .

 $\tau_{\rm c}$ leads to a weakening and broadening of $J_{\rm eff}(\omega)$. The dependence of $\tau_{\rm c}$ on the VSC rate constant profile resonance peak is dictated by the shape of $J_{\rm eff}(\omega)$, as shown in Fig. 4b. Under the lossless limit ($\tau_{\rm c} \to \infty$), there is no apparent cavity modification effect, as discussed in the previous work in Ref. 25. When gradually decrease the cavity lifetime, the resonance structure in the rate profile shows up and the VSC modifications gradually increase.

This trend is in line with the results in Ref. 25 using a similar model, where the cavity mode q_c was included in the quantum subsystem system description using Fock states. The rate constant enhancement reaches a maximum intensity when $\tau_c \approx 200$ fs, in which the rate constant is enhanced by 1.35 times. Further decreasing τ_c leads to a decreased and broadened rate constant profile. The cavity modification effect gradually disappears at the heavy loss limit $\tau_c \to 0$.

Fig. 4c further presents the peak value of k/k_0 (at $\omega_c = \omega_0$) as a function of cavity lifetime τ_c . One can see that the k/k_0 increase as the cavity lifetime increase, and then decrease, giving rise to a turnover when increasing τ_c , and In Ref. 25, For $\tau_c > 200$ fs (toward the lossless limit of $\tau_c \to \infty$), the cavity modification effects gradually decrease, agreeing with the previous results in Ref. 25. The trend of k/k_0 increase as τ_c increase for $\tau_c \in [0, 100]$ fs was not discussed in the previous literature. The current results bring a more complete picture of how k/k_0 depends on τ_c .

Using the FGR theory in Eq. 41, we can try to understand the basic scaling relation of the VSC-modified rate constant with respect to the cavity lifetime τ_c near the lossy limit, for $\tau_c \in [0, 200]$ fs. Under the resonance condition $\omega_c = \omega_0$ and the Markovian limit (Eq. 14), the $J_{\text{eff}}(\omega_0)$ term becomes

$$J_{\text{eff}}(\omega_0) = 2\eta_c^2 \omega_0^2 \tau_c, \tag{51}$$

which will be the predominant part of τ_c -dependence in the FGR rate of Eq. 44. This means that

$$k/k_0 \propto 1 + 4|\Delta_x|^2 \eta_c^2 \omega_0^2 \tau_c \cdot e^{-\beta \omega_0}/k_0.$$
 (52)

The above expression correctly predicts that under the $\tau_{\rm c} \to 0$ limit, $k/k_0 \to 1$, as we observed in HEOM simulations. It also correctly predicts the trend that k/k_0 increases as $\tau_{\rm c}$ increases. However, this expression will break down when $\tau_{\rm c} > 200$ fs, as is shown in the HEOM simulations (see Fig. 5d).

For the non-Markovian photon-loss bath²⁵ the basic trend will be similar. In this case, as $\tau_{\rm c}$ decreases, a blue shift will appear in $J_{\rm eff}(\omega)$, due to a non-negligible $\tilde{R}(\omega)$ (Eq. 12). The FGR rate (Eq. 41), on the other hand, will have a profile dictated by

$$J_{\rm eff}(\omega_0) = \frac{2\eta_{\rm c}^2\omega_{\rm c}^3J_{\rm c}(\omega_0)}{[\omega_{\rm c}^2 - \omega_0^2 + \tilde{R}(\omega_0)]^2 + [J_{\rm c}(\omega_0)]^2},$$

which peaks at $\omega_c = \sqrt{\omega_0^2 - \tilde{R}(\omega_0)}$. Thus, the peak of the rate profile will have a redshift, with the magnitude

$$\Delta\omega = \omega_0 \cdot \left(1 - \sqrt{1 - \tilde{R}(\omega_0)/\omega_0^2}\right). \tag{53}$$

Intuitively, this is because the peak of $J_{\rm eff}(\omega)$ should match the quantum transition frequency ω_0 to maximally enhance the $|\nu_{\rm L}\rangle \rightarrow |\nu'_{\rm L}\rangle$ transition. Since the non-Markovian spectral density is blue-shifted compared

to the Markovian case, one should expect $\omega_c < \omega_0$ in order to have the peak of $J_{\rm eff}(\omega)$ showing up at ω_0 . Thus, the resonance condition is red-shifted as $\omega_c = \sqrt{\omega_0^2 - \tilde{R}(\omega_0)}$. Note that this shift is purely due to the non-Markovian behavior of the photon-loss bath (which has nonzero $\tilde{R}(\omega_0)$). The numerical simulation with the non-Markovian photon-loss bath can, in principle, be performed using the recently developed time-domain Prony fitting decomposition scheme.⁷⁴

E. Numerical Behavior of $k_{ m VSC}$ in Eq. 41

So far, we have used the FGR theory in Eq. 44 to qualitatively interpret the VSC rate constant modifications, explain the resonance condition $\omega_{\rm c} = \omega_0$, the basic scaling rule of $k/k_0 \propto 1 + C \cdot \eta_c^2$, as well as the τ_c dependence of k/k_0 . Here, we assess the quantitative accuracy of the FGR rate constant in Eq. 41. Note that we are less interested in how to compute the rate outside the cavity k_0 , as there are many accurate theories to describe it in theoretical chemistry. 19,47,52,75 Rather, we want to focus on the performance of $k_{\rm VSC}$ in Eq. 41. As such, we only report the value of $k/k_0 = 1 + k_{\rm VSC}/k_0$, where we numerically integrate out $d\omega$ in Eq. 41 to obtain k_{VSC} , and we directly use the numerical result of $k_0 = 1.2672 \times 10^{-7}$ a.u.⁻¹ obtained from the HEOM simulation (outside cavity case in Fig. 3a). We used Eq. A21 to evaluate the convolution integral in Eq. 41, and compare the FGR rate constant with the HEOM results. We found that the simple FGR rate constant overestimates the results by 2.5 times compared to the numerically exact results obtained from HEOM, and will breakdown for large η_c and τ_c . Nevertheless, this simple FGR theory captures the basic trend of the VSC modified rate constant when $\eta_{\rm c} < 0.05$ (or $\Omega_{\rm R} < 25~{\rm cm}^{-1}$) and $\tau_{\rm c} < 100~{\rm fs}$, as shown in Fig. 5.

Fig. 5a presents the cavity frequency dependence of the VSC-modified rate profile, with the same parameters used in Fig. 3b. The open circles and the guiding thin lines are results obtained from the HEOM simulations (identical to those presented in Fig. 3b), and the thick solid lines are the results obtained from the FGR expression using Eq. 41 scaled by a factor of 0.4. Although not in perfect agreement, the FGR rate exactly predicted the resonant behavior at $\omega_c = \omega_0$, and provided semi-quantitative estimations for the peak height and width of the rate profile, when the light-matter coupling strength $\eta_c < 0.05$ (or $\Omega_R < 25$ cm⁻¹). For $\eta_c > 0.05$, the FGR expression still provides the resonant behavior but is further deviating from the HEOM results in terms of the magnitude due to the breakdown of FGR.

Fig. 5b presents the scaling relation between k/k_0 (at $\omega_c = \omega_0$, resonant condition) and the light-matter coupling strength η_c . The open red circles represent the results obtained from the HEOM simulations (identical to Fig. 3c). The red curve is a fitting line for data points when $\eta_c < 0.05$ (or $\Omega_R < 25$ cm⁻¹). The results ob-

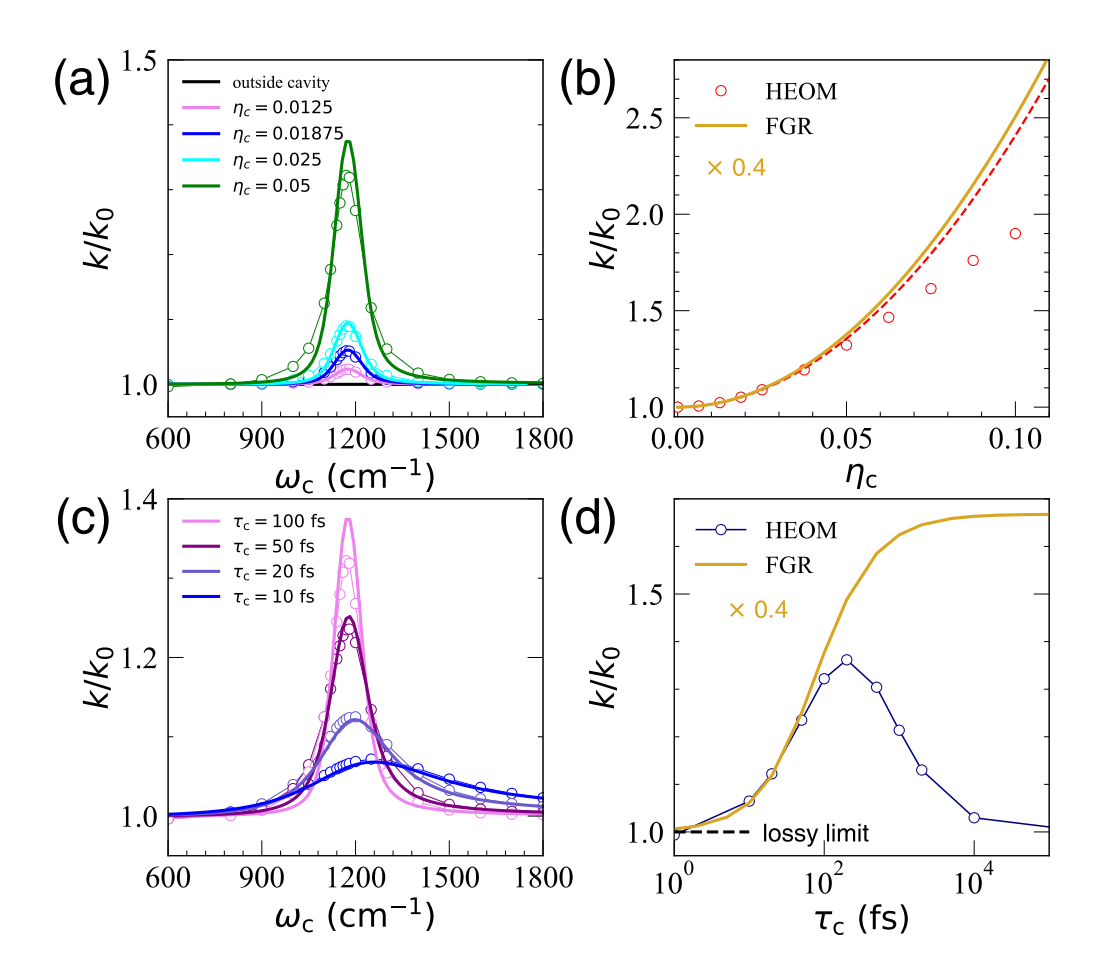


FIG. 5. Comparison between the numerically exact HEOM rate constants (open circles) and the FGR rate using Eq. 41 (solid lines) for VSC effect on k/k_0 . The FGR rate was multiplied by a factor of 0.4. (a) Resonance effect of VSC when changing the cavity frequency ω_c at various light-matter coupling strengths η_c . (b) k/k_0 with increasing η_c , with the results obtained from HEOM (red open circles) and FGR (golden curve). The rest of the parameters are identical to those in Fig. 3, and the red dashed line is the fitting of the HEOM data for $\eta_c < 0.05$. (c) Resonance effect of VSC when changing the cavity frequency ω_c at various cavity lifetimes τ_c . (d) k/k_0 with an increasing τ_c , obtained from HEOM (blue open circles) and FGR (golden line).

tained from FGR (Eq. 41) are presented with a solid gold line. The FGR rate, not surprisingly, correctly predicted $k/k_0 \propto \eta_c^2$ when $\eta_c < 0.05$ (or $\Omega_R < 25$ cm⁻¹). Further increasing η_c leads to a breakdown of the FGR, because it is only valid when $\Omega_{\rm R} \ll k_{\rm B}T$, where the Rabi splitting $\Omega_{\rm R}$ (Eq. E3) is the energy coupling term in the FGR (see Eq. E4). For the current model system, when $\Omega_{\rm R} < 25$ ${\rm cm}^{-1}$ ($\eta_{\rm c} < 0.05$), FGR provides an accurate description of the basic scaling of k/k_0 . With a further increase of $\Omega_{\rm R}$, the HEOM results suggests a scaling $k/k_0 \propto \eta_{\rm c}^n$, where n < 2 for the range of $\eta_c \in [0.05, 0.1]$. Experimentally, the typical range^{1,4} of Ω_R are within 200 cm⁻¹, and will likely observe $k/k_0 \propto 1 + \eta_c^n$ for $n \leq 2$. Our HEOM results also suggest that further increase in the light-matter coupling strength η_c will eventually lead to a saturation in the enhancement, in agreement with the previous study.²⁵

Fig. 5c presents the VSC-modified rate profile as a function of ω_c , by varying cavity lifetime τ_c using the same parameters as in Fig. 4. The open circles (and

the guiding thin lines) represent the results obtained from HEOM simulations (identical to those in Fig. 4b), whereas the thick solid lines are results obtained from FGR (Eq. 41). Note that the FGR results are also scaled by a factor of 0.4 to provide a convenient comparison with the HEOM results. Although not perfectly reproducing the numerically exact results, the FGR rate indeed captured the basic trend of the rate profile as one gradually increases $\tau_{\rm c}$ for $\tau_{\rm c} < 100$ fs.

Fig. 5d presents the k/k_0 at the resonant condition $\omega_c = \omega_0$, as a function of the cavity lifetime τ_c . The convolved FGR expression (Eq. 41) correctly captures the linear dependence of k/k_0 at small τ_c (< 100 fs) (as also predicted by Eq. 52). When further increase τ_c , the current FGR theory predicts that the rate profile gradually converges to a Gaussian line shape with a variance of σ^2 (see Eq. 43), resulting in a sigmoid dependence of k/k_0 as increasing τ_c (golden curve). The numerical simulations from HEOM (blue open circles), on the other hand, show a turnover behavior and start to deviate FGR for

 $\tau_{\rm c} > 100$ fs, indicating the breakdown of the current FGR theory. This is because under the lossless limit, the cavity loss no longer plays the role of a simple (homogeneous) broadening factor, but rather the photon number excitation (see Sec. E for details). Near the lossless limit, decreasing $\tau_{\rm c}$ induces a stronger cavity mode-photon loss coupling (see Eq. 13), thus a faster $|0\rangle \rightarrow |1\rangle$ transition (for the cavity Fock states). As a result, the resonance enhancement is magnified. Rate theories that describe this interesting behavior remain to be further developed.

As such, we conclude that the FGR expressions in Eq. 41 (as well as the small τ_c limit in Eq. 44) are theoretically valuable because they predict the correct scaling relations and semiquantitatively predict the accurate VSC-modified rate constants. Nevertheless, the numerical behavior of the FGR expression is not perfect, as one can see that it will overestimate the rate by 2.5 times for the model system we studied when FGR is valid, and will eventually breakdown for large light-matter coupling strength η_c and large cavity lifetime τ_c . That said, when FGR is valid, the rate expression provides a nearly perfect trend when changing ω_c , η_c , and τ_c .

IV. CONCLUDING REMARKS

Computational Approaches and Novelty. We performed numerically exact simulations using hierarchical equations of motion (HEOM) to investigate the effect of vibrational strong coupling (VSC) on the reaction rate constant. With harmonic analysis for the equations of motion, an effective spectral density function was derived to describe the cavity and its associated loss. In the HEOM simulations, only the system's vibrational states were described as the quantum subsystem, whereas the influence of the molecular phonon bath, the cavity mode, and its associated photon-loss bath were described implicitly using spectral density functions. Compared to recent work that treats the photon coordinate \hat{q}_c inside the quantum subsystem and using Fock state description, the current approach describes the cavity mode using an effective spectral density and thus significantly reduces the computational cost due to a much smaller number of states in the quantum subsystem. On the other hand, including \hat{q}_c in the quantum subsystem using Fock states does require truncation of the Fock states, while the current approach that treats $\hat{q}_{\rm c}$ inside the spectral density description does not explicitly involve any Fock state truncation. With this new description, it becomes possible to extend numerical exact simulations to multimode cases and polymeric systems with arbitrary types of bath TCF, even though in this work we are still under the single-molecule case. Another interesting direction of applying the current approach is to explore the quantum dynamics of a hybrid plasmonic-photonic structure that has few-Mode field quantization with structured spectral densities.⁷⁶

Origin of the Resonance Condition. Our numer-

ical simulations confirm the results in a recent work²⁵ which also performs exact quantum dynamics, suggesting that in the energy diffusion-limited regime of chemical reactions, the cavity mode acts like a "rate-promoting vibration (RPV) mode". 48 This "rate-promoting" cavity mode promotes the transition from the reactant ground vibrational state $|\nu_{\rm L}\rangle$ to the reactant excited vibrational state $|\nu'_{\rm I}\rangle$, then follows by tunneling to the product vibrational excited state $|\nu'_{\rm R}\rangle$, and eventually relaxes to the product ground vibrational state $|\nu_{\rm R}\rangle$. Our exact quantum dynamics results (Fig. 2) suggest that the presence of a resonant cavity mode whose frequency ω_c matches the quantum transition frequency ω_0 (corresponding to the $|\nu_{\rm L}\rangle \rightarrow |\nu_{\rm L}'\rangle$ transition) will significantly enhance the steady-state populations of the $|\nu'_{\rm L}\rangle$ and $|\nu'_{\rm R}\rangle$ states, thus promoting the forward rate constant.

The VSC-modified rate profile scanned as a function of the cavity frequency ω_c also shows a very sharp resonant feature (Fig. 3b), similar to the absorption spectra of the molecule outside the cavity (Fig. 3d).^{4,25} This is because both profiles originate from the same type of transition $|\nu_L\rangle \rightarrow |\nu_L'\rangle$. In optical absorption spectra, the laser frequency must match ω_0 to generate the optical excitation $|\nu_L\rangle \rightarrow |\nu_L'\rangle$, whereas in VSC-modified reactions, the cavity frequency ω_c must match ω_0 to efficiently promote the $|\nu_L\rangle \rightarrow |\nu_L'\rangle$ transition (under thermal condition).

Note that this quantum frequency ω_0 (Eq. 25) is different from the classical bottom of the well frequency $\omega_0^{\rm cl}$ (Eq. 26) or top of the barrier frequency $\omega_{\rm b}$ (Eq. 21) for an anharmonic potential. Previous work that uses classical rate theory to study VSC effects cannot find the resonance behavior of $\omega_{\rm c} = \omega_0$, because these theories rely on the classical description of the system (such as trajectories) which are sensitive to the classical frequencies of the potential. More detailed discussions of these previous classical rate theories for VSC can be found in Appendix E. In this sense, the proper description of the VSC resonance effect needs a quantum description that provides the quantum frequency information ω_0 (by providing the eigenenergies of the vibrational states).

Behavior of the VSC-modified Rate Constants. We further explored how the VSC-modified rate constant would be influenced by the light-matter coupling strength $\eta_{\rm c}$ (Eq. 7) and by the cavity lifetime $\tau_{\rm c}$ (Eq. 32). Our numerical results suggested that as η_c increased, the VSCmodified rate constant also increased, and a numerical fitting suggested that the rate constant enhances quadratically with η_c when $\eta_c < 0.05$ (or $\Omega_R < 25$ cm⁻¹, red curve in Fig. 3c). Using this observation, we also find that the modification of the free energy barrier does not scale linearly with the Rabi splitting $\Omega_{\rm R}$, but rather exhibits a logarithmic scaling of Ω_R (blue curve in Fig. 3c). This numerical behavior exhibits the essential feature of the nonlinear relationship between Ω_R and the modification of the free energy barrier.^{3,4,7} Although there are not many experimental studies on the relationship between VSC-modified rate constants and light-matter coupling strength, there is experimental evidence suggesting

a nonlinear relation between the rate constant and the light-matter coupling strength (Rabi splitting) in Ref. 4. Further experimental efforts are needed to investigate the scaling relation between the VSC rate constant and the light-matter coupling strength.

Furthermore, we explored how the cavity loss or the cavity lifetime, τ_c , influences the VSC effects. We find that the VSC modified rate constant in Fig. 4 exhibits a turnover profile from the lossless limit $(\tau_c \to \infty)$ to the lossy limit $(\tau_c \to 0)$, and the rate constant peaks at a particular τ_c . To the best of our knowledge, there is no experimental work that reports how VSC-modified rate constant changes as a function of τ_c . There is an interesting experiment that measures the exciton-polariton diffusion rate constant with changing τ_c , suggesting a decrease in τ_c will diminish the diffusion rate constant. Thus, future experiments on checking how VSC-modified rate constant changes with respect to the quality factor of cavities will be needed, even for those reactions that are already reported.^{4,5}

Analytic Theory of VSC Rate Constant. Noticing the steady-state behavior of the population dynamics for $|\nu_{\rm L}'\rangle$ and $|\nu_{\rm R}'\rangle$ (red and green curves in Fig. 2), we apply the steady-state approximation to the kinetics (Eq. 38) and concluded that the overall forward rate constant is identical to the rate constant of the $|\nu_{\rm L}\rangle \rightarrow |\nu_{\rm L}'\rangle$ transition. Using Fermi's Golden Rule (FGR) to evaluate this rate, we arrived at an analytical expression of the VSC-modified rate constant for the system investigated in this work (cf. Eq. 41)

$$k_{\rm VSC} = 2|\Delta_x|^2 \int_0^\infty d\omega \ J_{\rm eff}(\omega) \cdot G(\omega - \omega_0) \cdot n(\omega).$$
 (54)

On the other hand, a less accurate but more intuitive expression of $k_{\rm VSC}$ is available under the zero-phonon broadening limit $G(\omega - \omega_0) \to \delta(\omega - \omega_0)$ and the Markovian limit for $J_{\rm eff}(\omega)$ (see Eq. 14), resulting in (cf. Eq. 44)

$$k_{\rm VSC} \approx 2|\Delta_x|^2 \cdot \frac{2\alpha\eta_{\rm c}^2\omega_{\rm c}^3\omega_0}{(\omega_{\rm c}^2 - \omega_0^2)^2 + \alpha^2\omega_0^2} \cdot n(\omega_0).$$
 (55)

The above FGR expression, although quantitatively less accurate, can already be used to qualitatively understand the resonant behavior of the VSC-modified rate profiles in Fig. 3b and Fig. 4b, which gives rise to a maximum rate enhancement when $\omega_{\rm c} = \omega_0$. With this simple FGR rate, we can also understand the observed scaling relation of $k_{\rm VSC} \propto \eta_{\rm c}^2$ (Fig. 3c), as well as the basic trend that $k_{\rm VSC} \to 0$ when $\tau_{\rm c} = 1/\alpha \to 0$. As such, the FGR expression in Eq. 54 and its simpler limit in Eq. 55 provide a resonant VSC theory that can explain most of the numerical results in our work. To the best of our knowledge, this is the first analytic theory to explain the resonance enhancement of the VSC rate constant for an electronically adiabatic reaction.¹⁰ Despite its success in terms of explaining all basic trends of the VSC-modified rate constant (as shown in Fig. 5), the current expression overestimates the absolute rate constant by a factor

of 2.5. Future work is needed to develop a more quantitatively accurate rate constant for VSC-modified chemistry, as well as for the stronger light-matter coupling regime $(\eta_c>0.05)$ and for the lossless case $(\tau_c>200~\mathrm{fs}).$

Summary of Key Predictions. Based on current numerical results and the analytic FGR rate constant expression, we provide the following predictions. All of these, of course, are limited to the single molecule coupled to the cavity.

- [1]. The current work predicts that the VSC-enhanced rate effect should scale as $k/k_0 \propto 1 + \mathcal{C} \cdot (\Omega_{\rm R}/2\omega_{\rm c})^2$, i.e., increasing Rabi splitting $\Omega_{\rm R}$ will quadratically enhance the VSC-modified rate constant. As a corollary, the effective free energy barrier change scales as $\Delta(\Delta G^{\ddagger}) \propto -k_{\rm B}T \ln\left[1 + \mathcal{C} \cdot (\Omega_{\rm R}/2\omega_{\rm c})^2\right]$, which is a nonlinear function of $\Omega_{\rm R}$, consistent with the recent experimental observation.⁴
- [2]. The $k_{\rm VSC}$ for isotropic dipole orientation (see Eq. 47) is three times smaller than the $k_{\rm VSC}$ in Eq. 41 for fully aligned case. In general, if one can experimentally control the distribution of the orientation of the dipole^{77,78}, then the general scaling should be $k_{\rm VSC} \propto \langle \cos^2 \varphi \rangle$, due to the FGR theory that depends on the coupling squared matrix.
- [3]. The FWHM of the rate profile is controlled by a convolution of $J_{\rm eff}(\omega)$ and a broadening function, whose FWHMs are $\alpha=2\lambda_c/\gamma_c$ (Eq. 30) and $\sigma^2\propto \int_0^\infty d\omega\ J_\nu(\omega) \coth(\beta\omega/2)$ (Eq. A6), respectively. This is almost in perfect agreement with the numerical results (see Fig. 5c) for a small lifetime of the cavity when $\tau_c<100$ fs (see Fig. 5).
- [4]. The current numerically exact results predict that there will be a turnover of the rate constant as one increases the cavity lifetime $\tau_{\rm c}$. As the cavity lifetime $\tau_{\rm c}$ increases, the VSC effect will increase first, which agrees with the analytic FGR theory. When further increasing the $\tau_{\rm c}$, the numerically exact simulation suggests that the cavity modification effects decay to zero, ²⁵ and the analytic FGR theory failed to predict this trend. On the other hand, both numerical results and the analytic FGR theory predict that the cavity effect will diminish when $\tau_{\rm c} \to 0$ for a very lossy cavity.
- [5]. The VSC enhancing effect will saturate with an increasing light-matter coupling strength η_c (or Rabi splitting Ω_R), such that $k_1 \gg k_2, k_3$, which breaks the mechanistic assumption that based on steady-state approximation. Related to this, for two chemically similar reactions, if one satisfies $k_1 \ll k_2, k_3$ but the other does not, then the current theory predicts that there will be a VSC effect for the first reaction but not for the second one.

We hope that the current theory and predictions can offer valuable insights into the fundamental mechanism of vibrational polariton chemistry, be useful for near future experimental measurements to carefully check how the VSC-modified rate constant changes by varying different parameters, even for those VSC-modified chemical reactions^{1,4,5} that have already been reported.

Limitation and Future Directions. Despite sev-

eral initial successes of the FGR theory (Eq. 41) and the quantum dynamics simulations, obviously, there are several limitations in the current work.

- [1]. The current theory and simulation assume that a single molecule is coupled to the cavity. On the other hand, the VSC experiments operate under a collective coupling regime, such that an estimated $N = 10^6 \sim 10^{10}$ molecules are collectively coupled to the FabryPérot cavity for each cavity mode. 10,11,14,79 This means that the light-matter coupling strength η_c is really weak between individual molecules and the cavity, and the experimentally observed Rabi splitting will be $\Omega_{\rm R} \propto \sqrt{N\eta_{\rm c}}$. Further, under the collective coupling regime, it is expected that the molecular orientations are isotropically distributed. Note that by considering fully isotropically distributed dipoles, classical rate theory predicts that there are no VSC effects. 14,22 The furture theoretical development is needed to understand the collective effect when considering the isotropic dipole distribution.
- [2]. The current theory assumes only one cavity mode, whereas in the FabryPérot cavity, there are many cavity modes. 12,80,81 For a k_{\perp} mode that satisfies mirror boundaries, there will be continuous choices of k_{\parallel} , such that the photon energy is $\omega_{\bf k} \propto \sqrt{k_{\parallel}^2 + k_{\perp}^2}$. Experimentally, only when $\omega_{\bf k} = \omega_0$ at $k_{\parallel} = 0$ is satisfied can one observe VSC modification on the rate constant. For a given finite k_{\parallel} , it is possible for $\omega_{\bf k} = \omega_0$, but there will be no apparent VSC effect. 6,7,79
- [3]. The current work focuses on the VSC enhancement effect^{4,5} where the reaction is originally in the energy diffusion-limited regime (low friction regime before the Kramers turnover¹⁹). Although we have not discussed VSC-suppressed reactivity, the cavitysuppressed steady-state population and the rate constant k_1 have been observed in classical and quantum simulations^{21,26,82,83}, when the molecular system is originally under the high friction limit (after Kramers turnover^{19,84}, or the so-called spatial diffusion-limited regime). We anticipate that the current theory and simulations will also likely be able to produce the resonance suppression effect if the reaction is originally sitting in the spatial diffusionlimited regime.

As nicely summarized in a recent review, 10 no existing theory can simultaneously explain the resonance effect $(\omega_c = \omega_0)$, the collective effect (limitation 1), the $k_{\parallel} = 0$ condition (limitation 2), and survive under the isotropic orientation of dipoles (limitation 1). In the future, we aim to generalize the current observation and the rate theory to explicitly address these above-mentioned limitations and provide a microscopic theory to successfully explain all observed VSC phenomena.

SUPPLEMENTARY MATERIAL

See Supplementary Material for additional Information on the theoretical details of Hierarchical equations

of motion; details of computing Infrared spectra of the bare-molecule system; summary of parameters; matter subspace construction and convergence test.

ACKNOWLEDGMENTS

This work was supported by the National Science Foundation Award under Grant No. CHE-2244683. P.H. appreciates the support of the Cottrell Scholar Award (a program by the Research Corporation for Science Advancement). Computing resources were provided by the Center for Integrated Research Computing (CIRC) at the University of Rochester. P.H. and W.Y. appreciate extremely valuable discussions with Arkajit Mandal and Mike Taylor. W. Y. is in debt to Zi-Hao Chen for his tremendous help in coding and would also like to sincerely thank Yifan Lai, Elious Mondal, Xinxian Chen and Yao Wang for valuable discussions and comments on the manuscript.

DATA AVAILABILITY

The data that support the findings of this work are available from the corresponding author under reasonable request.

Appendix A: Derivation of the FGR rate constant in Eq. 41

We want to provide a quantitative evaluation of the FGR rate constant in Eq. 41, which requires to explicitly evaluate the coupling term $\langle \nu_{\rm L}'|\hat{H}|\nu_{\rm L}\rangle$.

We begin by writing down the coupling term using the total Hamiltonian in Eq. 17-18, leading to

$$\langle \nu'_{L} | \hat{H} | \nu_{L} \rangle = (\lambda_{\nu} + \lambda_{\text{eff}}) \cdot \langle \nu'_{L} | \hat{R}^{2} | \nu_{L} \rangle + \langle \nu'_{L} | \hat{R} | \nu_{L} \rangle \cdot (\hat{F}_{\nu} + \hat{F}_{\text{eff}}), \tag{A1}$$

where $\langle \nu_{\rm L}' | \hat{H}_{\rm S} | \nu_{\rm L} \rangle = 0$ (because of the orthogonality of $\{|\nu_0\rangle, |\nu_1\rangle\}$ and $\{|\nu_2\rangle, |\nu_3\rangle\}$ subspaces), and $\langle \nu_{\rm L}' | \hat{h}_{\rm B}^{\rm eff} | \nu_{\rm L} \rangle = 0$ (due to no \hat{R} operator in this term). The first term in Eq. A1 originates from reorganization energy term $\hat{H}_{\rm ren}$, and the second term originates from the $\hat{H}_{\rm SB}$. Details about the matrix representation of the relevant terms can be found in Sec. II of the Supplementary Material. Here we aim to establish a rate expression for the coupling terms described in Eq. A1.

With this, we focus on the subspace spanned by $\{|\nu_{\rm L}\rangle, |\nu'_{\rm L}\rangle\}$, the total Hamiltonian \hat{H} (Eq. 18) in this projected subspace $\hat{\mathcal{P}} = |\nu_{\rm L}\rangle\langle\nu_{\rm L}| + |\nu'_{\rm L}\rangle\langle\nu'_{\rm L}|$ is $\hat{\mathcal{H}} = \hat{\mathcal{P}}\hat{H}\hat{\mathcal{P}}$, which is expressed as

$$\hat{\mathcal{H}} = \omega_0 |\nu_{\rm L}'\rangle\langle\nu_{\rm L}'| + \hat{H}_{\rm ren} + \hat{h}_{\rm B}^{\rm eff}
+ R_{\rm LL'}(|\nu_{\rm L}\rangle\langle\nu_{\rm L}'| + |\nu_{\rm L}'\rangle\langle\nu_{\rm L}|) \otimes (\hat{F}_{\nu} + \hat{F}_{\rm eff})
+ (R_{\rm LL}|\nu_{\rm L}\rangle\langle\nu_{\rm L}| + R_{\rm L'L'}|\nu_{\rm L}'\rangle\langle\nu_{\rm L}'|) \otimes (\hat{F}_{\nu} + \hat{F}_{\rm eff}),$$
(A2)

where $\hat{H}_{\rm ren}$ and $\hat{h}_{\rm B}^{\rm eff}$ are defined in Eq. 18, \hat{F}_{ν} and $\hat{F}_{\rm eff}$ are defined in Eq. 19, and we have subtracted out zero point energy \mathcal{E}). The numerical values of the matrix elements for our current model are $R_{\rm LL'} = \langle \nu_{\rm L} | \hat{R} | \nu_{\rm L}' \rangle = 0.214$ a.u., $R_{\rm LL} = \langle \nu_{\rm L} | \hat{R} | \nu_{\rm L} \rangle = -0.933$ a.u., and $R_{\rm L'L'} = \langle \nu_{\rm L}' | \hat{R} | \nu_{\rm L}' \rangle = -0.702$ a.u., and we have found numerically that $\lambda_{\rm eff} \ll \lambda_{\nu}$ for all light-matter coupling strength $\eta_{\rm c}$ that we have considered in this work (see Sec. II of the Supplementary Material), and we thus explicitly set $\lambda_{\rm eff} = 0$ in our following analysis. In Eq. A2, the second line describes Peierls-type of system-bath coupling (off-diagonal couplings) which includes both the phonon and the photon fluctuations, in which the term

$$R_{\mathrm{LL'}}(|\nu_{\mathrm{L}}\rangle\langle\nu_{\mathrm{L}}'| + |\nu_{\mathrm{L}}'\rangle\langle\nu_{\mathrm{L}}|) \otimes \hat{F}_{\mathrm{eff}}$$
 (A3)

should be responsible for the VSC resonance enhancement effects, and will be treated by FGR rate theory. The third line in Eq. A2 describes Holstein-type of systembath coupling (diagonal coupling), in which the term

$$(R_{\rm LL}|\nu_{\rm L}\rangle\langle\nu_{\rm L}| + R_{\rm L'L'}|\nu'_{\rm L}\rangle\langle\nu'_{\rm L}|) \otimes \hat{F}_{\nu}$$
 (A4)

is mainly responsible for the inhomogeneous broadening effect in spectra. The other terms, among which $\hat{H}_{\rm ren}$, $R_{\rm LL'}(|\nu_{\rm L}\rangle\langle\nu_{\rm L}'|+|\nu_{\rm L}'\rangle\langle\nu_{\rm L}|)\otimes\hat{F}_{\nu}$ simply does not belong to the definition of net rate enhancement $(k_{\rm VSC})$, and $(R_{\rm LL}|\nu_{\rm L}\rangle\langle\nu_{\rm L}|+R_{\rm L'L'}|\nu_{\rm L}'\rangle\langle\nu_{\rm L}'|)\otimes\hat{F}_{\rm eff}$ is less important due to its much smaller magnitude, are thus discarded from our following discussions.

Consequently, Eq. A2 can be simplified and written in the pseudo-spin representation as $\,$

$$\hat{\mathcal{H}} = \omega_0 \frac{\hat{\sigma}_z}{2} + \hat{\mathcal{P}} \otimes \hat{F}_{\text{eff}} + \hat{h}_{\text{B}}^{\text{eff}}$$

$$+ \Delta_x \hat{\sigma}_x \otimes \hat{F}_{\text{eff}} + \epsilon_z \frac{\hat{\sigma}_z}{2} \otimes \hat{F}_{\nu}$$
(A5)

where $\hat{\sigma}_z = |\nu_{\rm L}'\rangle\langle\nu_{\rm L}'| - |\nu_{\rm L}\rangle\langle\nu_{\rm L}|$, and $\hat{\sigma}_x = |\nu_{\rm L}\rangle\langle\nu_{\rm L}'| + |\nu_{\rm L}'\rangle\langle\nu_{\rm L}|$. Further, $\Delta_x = R_{\rm LL'} = 0.214$ a.u., $\epsilon_z = R_{\rm L'L'} - R_{\rm LL} = 0.231$ a.u.. The first line of Eq. A5 does not involve the light-matter coupling, and the second line of Eq. A5 is the one responsible for cavity modification effects. Noticing that the light-matter coupling term $\hat{F}_{\rm eff}$ explicitly shows up in the coupling between the $|\nu_{\rm L}\rangle$ and $|\nu_{\rm L}'\rangle$, which is not a constant.

The coupling term $(\epsilon_z \hat{\sigma}_z/2) \otimes \hat{F}_{\nu}$ will fluctuate the energy difference between $|\nu_{\rm L}\rangle$ and $|\nu_{\rm L}'\rangle$. We account for this additional fluctuation as the static disorder (inhomogeneous broadening), because of the low phonon frequencies of \hat{H}_{ν} . The variance of this fluctuation is^{85–87}

$$\sigma^2 = \epsilon_z^2 \cdot \frac{1}{\pi} \int_0^\infty d\omega \ J_\nu(\omega) \coth(\beta \omega/2), \qquad (A6)$$

which has a numerical value of $\sigma \approx 30.83 \text{ cm}^{-1}$ for our model under T = 300 K, calculated via numerical integration (see Ref. 78 for detailed illustrations).

With the above analysis, the rate constant is ready to be written down as 50

$$k_{\rm VSC} = \int_0^\infty d\omega \ \kappa(\omega) G(\omega - \omega_0),$$
 (A7)

where $\kappa(\omega)$ is the FGR rate constant for the $|\nu_{\rm L}\rangle \rightarrow |\nu_{\rm L}'\rangle$ transition at a given cavity frequency $\omega_{\rm c}$, expressed as⁸⁸

$$\kappa(\omega) = 2\pi \sum_{j} \sum_{\substack{n_{\text{b},j}^{\text{eff}} \\ \text{b},j}} |\langle \nu_{\text{L}}, n_{\text{b},j}^{\text{eff}} + 1 | \Delta_{x} \hat{\sigma}_{x} \otimes \hat{F}_{\text{eff}} | \nu'_{\text{L}}, n_{\text{b},j}^{\text{eff}} \rangle|^{2}$$

$$\times \frac{e^{-(n_{\text{b},j}^{\text{eff}} + 1)\beta\tilde{\Omega}_{j}}}{\mathcal{Z}_{\text{b}}^{\text{eff}}} \delta(\omega - \tilde{\Omega}_{j})$$

$$= 2\pi |\Delta_{x}|^{2} \sum_{j} \frac{\tilde{C}_{j}^{2}}{2\tilde{\Omega}_{j}} \delta(\omega - \tilde{\Omega}_{j}) \sum_{\substack{n_{\text{b},j}^{\text{eff}} \\ \text{b},j}} \frac{e^{-(n_{\text{b},j}^{\text{eff}} + 1)\beta\tilde{\Omega}_{j}}}{\mathcal{Z}_{\text{b}}^{\text{eff}}} (n_{\text{b},j}^{\text{eff}} + 1)$$

$$= 2|\Delta_{x}|^{2} \cdot J_{\text{eff}}(\omega) \cdot n(\omega), \tag{A8}$$

where we have defined the Bose-Einstein distribution function as below,

$$n(\omega) = \sum_{\substack{n_{\mathrm{b},j}^{\mathrm{eff}} \\ \mathbf{b},j}} \frac{e^{-(n_{\mathrm{b},j}^{\mathrm{eff}} + 1)\beta\tilde{\Omega}_{j}}}{\mathcal{Z}_{\mathrm{b}}^{\mathrm{eff}}} (n_{\mathrm{b},j}^{\mathrm{eff}} + 1) = \frac{1}{e^{\beta\omega} - 1}. \quad (A9)$$

In the last line of Eq. A8, we used the definition of the effective spectral density function (Eq. 11) which is in the discrete form. The broadening function $G(\omega - \omega_0)$ is a Gaussian distribution centered around ω_0 , defined as

$$G(\omega - \omega_0) = \frac{1}{\sqrt{2\pi\sigma^2}} \exp\left[-\frac{(\omega - \omega_0)^2}{2\sigma^2}\right].$$
 (A10)

In principle, one can use the convolution theorem to evaluate the expression in Eq. 41. As such, one just have to separately evaluate the Fourier transform of both κ and G, then multiply them together and inverse Fourier transform them to get the analytic answer of $k_{\rm VSC}$. Here, both $\kappa(\omega)$ and $G(\omega)$ are square-integrable functions, we can extend the integral to $-\infty$ by analytical continuation of $\kappa(\omega)$ and $G(\omega)$, and replace ω_0 with a variable ω , resulting in

$$k_{\rm VSC}(\omega) = \int_{-\infty}^{\infty} d\omega' \ \kappa(\omega') G(\omega - \omega') = \kappa(\omega) * G(\omega),$$
(A11)

where * denotes convolution. According to the convolution theorem,

$$\mathcal{F}^{-1}[\kappa(\omega) * G(\omega)] = 2\pi \mathcal{F}^{-1}[\kappa(\omega)] \cdot \mathcal{F}^{-1}[G(\omega)], \quad (A12)$$

where \mathcal{F}^{-1} denotes inverse Fourier transform. It is easy to get

$$\mathcal{F}^{-1}[G(\omega)] = \frac{1}{2\pi} \int_{-\infty}^{\infty} d\omega \ G(\omega) e^{-i\omega t} = \frac{1}{2\pi} e^{-\frac{\sigma^2 t^2}{2}}.$$
(A13)

On the other hand,

$$\mathcal{F}^{-1}[\kappa(\omega)] = \frac{|\Delta_x|^2}{\pi} \int_{-\infty}^{\infty} d\omega \, \frac{J_{\text{eff}}(\omega)}{e^{\beta\omega} - 1} e^{-i\omega t} \equiv |\Delta_x|^2 C_{\text{eff}}(t),$$
(A14)

where $C_{\rm eff}(t)$ is the effective TCF according to bosonic fluctuation-dissipation theorem. ⁴⁶ Unfortunately, we do not have a closed analytic form for $\mathcal{F}^{-1}[\kappa(\omega)]$. Nevertheless, one can still evaluate it numerically. Being in line with the HEOM formalism (see Sec. I of the Supplementary Material), if we assume that the effective TCF can be decomposed into a series of exponential decay basis, which means

$$C_{\text{eff}}(t) = \sum_{k} \eta_k e^{-\gamma_k t}.$$
 (A15)

This decomposition can usually be achieved by Matsubara spectral decomposition $(MSD)^{46}$ and Padé spectral decomposition $(PSD)^{89-91}$, or directly by various least-square fitting schemes^{74,92-95}. Then

$$2\pi \mathcal{F}^{-1}[\kappa(\omega)] \cdot \mathcal{F}^{-1}[G(\omega)] = |\Delta_x|^2 \sum_k \eta_k e^{-\frac{\sigma^2 t^2}{2} - \gamma_k t},$$
(A16)

whose Fourier transform reads as

$$\kappa(\omega) * G(\omega) = |\Delta_x|^2 \sum_k \eta_k \int_{-\infty}^{\infty} dt \ e^{-\frac{\sigma^2 t^2}{2} - (\gamma_k - i\omega)t}$$
$$= 2\pi |\Delta_x|^2 \sum_k \frac{\eta_k}{\sqrt{2\pi\sigma^2}} e^{\frac{(\gamma_k - i\omega)^2}{2\sigma^2}}. \tag{A17}$$

The VSC-modified rate profile takes the real part of Eq. A17, and $\omega = \omega_0$.

As a special example to do the decomposition in Eq. A15, direct discretization of the spectral density function will be a most convenient and accurate way to numerically evaluate Eq. A14, then the VSC rate of Eq. 41. Using the discrete definition of spectral density (cf. Eq. 11),

$$J_{\text{eff}}(\omega) = \frac{\pi}{2} \sum_{j} \frac{\tilde{C}_{j}^{2}}{\tilde{\Omega}_{j}} \delta(\omega - \tilde{\Omega}_{j}),$$

Eq. A14 is evaluated as

$$\mathcal{F}^{-1}[\kappa(\omega)] = \frac{|\Delta_x|^2}{2} \sum_j \frac{(\tilde{C}_j^2/\tilde{\Omega}_j)}{1 - e^{-\beta\tilde{\Omega}_j}} e^{-i\tilde{\Omega}_j t}.$$
 (A18)

Denoting

$$\eta_k = \frac{(\tilde{C}_k^2/\tilde{\Omega}_k)}{2(1 - e^{-\beta\tilde{\Omega}_k})}, \quad \gamma_k = i\tilde{\Omega}_k,$$
 (A19)

and plugging them into Eq. A17, one obtains

$$\kappa(\omega) * G(\omega) = \pi |\Delta_x|^2 \sum_j \frac{(\tilde{C}_j^2/\tilde{\Omega}_j)}{1 - e^{-\beta \tilde{\Omega}_j}} G(\tilde{\Omega}_j - \omega), \quad (A20)$$

which is purely real. As such,

$$k_{\text{VSC}} = \pi |\Delta_x|^2 \sum_j \frac{(\tilde{C}_j^2/\tilde{\Omega}_j)}{1 - e^{-\beta \tilde{\Omega}_j}} G(\tilde{\Omega}_j - \omega_0).$$
 (A21)

The above expression in Eq. A21 is equivalent to plugging the discrete spectral density expression $J_{\rm eff}(\omega) = \frac{\pi}{2} \sum_j \frac{\tilde{C}_j^2}{\tilde{\Omega}_j} \delta(\omega - \tilde{\Omega}_j)$ into Eq. A7 then explicitly evaluate the integral, which is not surprising. Instead of just using evenly distributed grid points in ω to evaluate the integral, ⁴⁰ the integral converges faster if one can efficiently sample the distribution of the frequencies $\{\tilde{\Omega}_j\}$ and coupling coefficients $\{\tilde{C}_j\}$ in the spectral density (Eq. 11) using strategies in Ref. 96 (or related earlier approaches in Ref. 47 and Ref. 97).

Appendix B: Reaction Rate Constant Analysis

The rate constant expression in Eq. 37 can be derived based on simple rate equations with the detailed balance relation between the forward and backward rate constants. Here, we briefly sketch the derivation following the work of Ref. 98. For a unimolecular reaction (reactant to product) that is reversible and governed by rate kinetics, one has

$$\frac{d}{dt}P_{\mathcal{R}}(t) = -\frac{d}{dt}P_{\mathcal{P}}(t) = -k_f P_{\mathcal{R}}(t) + k_b P_{\mathcal{P}}(t), \quad (B1)$$

where $P_{\mathcal{R}}(t)$ and $P_{\mathcal{P}}(t)$ are the populations of the reactant and product regions at time t, while k_f and k_b are the forward and backward reaction rate constants, respectively. When the reaction reaches equilibrium, $P_{\mathcal{R}}(t)$ and $P_{\mathcal{P}}(t)$ does not depend on time,

$$\frac{d}{dt}P_{\mathcal{R}}(t) = -\frac{d}{dt}P_{\mathcal{P}}(t) = 0,$$
(B2)

such that $k_b/k_f = \langle P_R \rangle/\langle P_P \rangle \equiv \chi_{\rm eq}$, where $\langle P_R \rangle$ and $\langle P_P \rangle$ denotes equilibrium populations of reactant and product. We also assume that the reactant and product regions can be described using the projection operators $1 - \hat{h}$ and \hat{h} , such that

$$\langle P_{\mathcal{R}} \rangle = \frac{1}{\mathcal{Z}} \text{Tr}[e^{-\beta \hat{H}} (1 - \hat{h})],$$
 (B3a)

$$\langle P_{\mathcal{P}} \rangle = \frac{1}{Z} \text{Tr}[e^{-\beta \hat{H}} \hat{h}],$$
 (B3b)

where \hat{H} is the total Hamiltonian, $\mathcal{Z} = \text{Tr}[e^{-\beta \hat{H}}]$ is the overall partition function. Eq. B1 can be rewritten as

$$\frac{d}{dt}P_{\mathcal{R}}(t) = -k_f P_{\mathcal{R}}(t) + k_f \chi_{\text{eq}}[1 - P_{\mathcal{R}}(t)]. \tag{B4}$$

Eq. B4 holds for the rate dynamics at a sufficient long time, entering into the rate process regime (linear response regime), *i.e.*, $t \rightarrow t_{\rm p}$ where $t_{\rm p}$ represents the

"plateau" time of the time-dependent rate. As a result, the forward rate constant can be expressed as

$$k_f = -\lim_{t \to t_p} \frac{\dot{P}_{\mathcal{R}}(t)}{P_{\mathcal{R}}(t) + \chi_{\text{eq}} \cdot [P_{\mathcal{R}}(t) - 1]}, \quad (B5)$$

giving rise to Eq. 37 of the main text. More generally, the non-equilibrium population at time t can be expressed as (cf. Eq. 35)

$$P_{\mathcal{R}}(t) = \text{Tr}_{\mathcal{S}} \left[e^{i\hat{H}t} (1 - \hat{h}) e^{-i\hat{H}t} \hat{\rho}_{\mathcal{S}}(0) \right], \quad (B6a)$$

$$P_{\mathcal{P}}(t) = \text{Tr}_{S} \left[e^{i\hat{H}t} \hat{h} e^{-i\hat{H}t} \hat{\rho}_{S}(0) \right].$$
 (B6b)

Then $\dot{P}_{\mathcal{R}}(t)$ can be evaluated from Eq. B6a as

$$\frac{d}{dt}P_{\mathcal{R}}(t) = \frac{d}{dt}\operatorname{Tr}_{S}\left[e^{i\hat{H}t}(1-\hat{h})e^{-i\hat{H}t}\hat{\rho}_{S}(0)\right]$$

$$= -\operatorname{Tr}_{S}\left[e^{i\hat{H}t}\hat{F}e^{-i\hat{H}t}\hat{\rho}_{S}(0)\right], \tag{B7}$$

where \hat{F} is the flux operator defined as

$$\hat{F} = i[\hat{H}, \hat{h}]. \tag{B8}$$

We further define the reactive flux correlation function $C_f(t)$ as

$$C_f(t) = -\frac{d}{dt} P_{\mathcal{R}}(t) = \text{Tr}_{S} \left[e^{i\hat{H}t} \hat{F} e^{-i\hat{H}t} \hat{\rho}_{S}(0) \right], \quad (B9)$$

then k_f in Eq. B5 is recast as

$$k_f = \lim_{t \to t_{\rm p}} \frac{C_f(t)}{P_{\mathcal{R}}(t) + \chi_{\rm eq} \cdot [P_{\mathcal{R}}(t) - 1]}.$$
 (B10)

In addition, we want to show the expression of the population of $|\nu_{\rm R}\rangle$ in Eq. 39 under the steady-state approximation. Following standard textbook derivation, we have the differential rate expression for the reaction scheme in Eq. 38 as follows,

$$\frac{d}{dt}[\nu_{\rm L}] = -k_1[\nu_{\rm L}],\tag{B11a}$$

$$\frac{d}{dt}[\nu'_{\rm L}] = k_1[\nu_{\rm L}] - k_2[\nu'_{\rm L}],$$
 (B11b)

$$\frac{d}{dt}[\nu_{R}'] = k_2[\nu_{L}'] - k_3[\nu_{R}'],$$
 (B11c)

$$\frac{d}{dt}[\nu_{\mathbf{R}}] = k_3[\nu_{\mathbf{R}}']. \tag{B11d}$$

The observed population dynamics in Fig. 2 indicates both $|\nu'_{\rm L}\rangle$ and $|\nu'_{\rm R}\rangle$ states reach to a steady-state during the dynamics, meaning that to a good approximation,

$$\frac{d}{dt}[\nu_{\rm L}'] = \frac{d}{dt}[\nu_{\rm R}'] = 0, \tag{B12}$$

for the majority of the dynamics (e.g., t > 3 ps for inside cavity case and t > 0.1 ps for outside cavity case), where the growth of population in $|\nu_{\rm R}\rangle$ also reaches to

a rate process. Eq. B12 is commonly referred to as the steady-state (ss) approximation, which allows us to set the time derivative of all intermediate states as 0. Using this approximation for $[\nu'_{\rm L}]$ and Eq. B11b, one has

$$[\nu'_{\rm L}] = \frac{k_1}{k_2} \cdot [\nu_{\rm L}] = \frac{k_1}{k_2} \cdot [\nu_{\rm L}(0)] \cdot e^{-k_1 t},$$
 (B13)

where the last equality is a result of integrating Eq. B11a with the initial condition $[\nu_L(0)] \neq 0$ and all the rest of populations equal to 0. The corresponding expression for $[\nu_R']$ under the steady-state approximation is

$$[\nu_{\rm R}'] = \frac{k_2}{k_3} \cdot [\nu_{\rm L}'] = \frac{k_1}{k_3} \cdot [\nu_{\rm L}(0)] \cdot e^{-k_1 t}.$$
 (B14)

Finally, plugging Eq. B14 into Eq. B11d, one has

$$\frac{d}{dt}[\nu_{R}] = k_{3}[\nu'_{R}] = k_{1} \cdot [\nu_{L}(0)] \cdot e^{-k_{1}t}.$$
 (B15)

Integrating the above equation results in the well-known results in Eq. 39.

Appendix C: Derivation of the effective spectral density

In this section, we follow the approach proposed by Leggett^{44} and Garg, et al.³⁸ to derive the expression of effective spectral density function. The linear systembath interaction mediated by a discrete boson can be described by the Hamiltonian as below,

$$\hat{H} = \frac{\hat{p}_{s}^{2}}{2M_{s}} + V(\hat{q}_{s}) + \frac{\hat{p}_{c}^{2}}{2} + \frac{1}{2}\omega_{c}^{2}(\hat{q}_{c} + \zeta\hat{q}_{s})^{2} + \frac{1}{2}\sum_{j} \left[\hat{\tilde{p}}_{j}^{2} + \tilde{\omega}_{j}^{2}\left(\hat{q}_{j} - \frac{\xi\tilde{c}_{j}}{\tilde{\omega}_{j}^{2}}\hat{q}_{c}\right)^{2}\right], \quad (C1)$$

where $\hat{q}_{\rm s}$, $\hat{p}_{\rm s}$ are the conjugated coordinate-momentum pair of the system DOF; $\hat{q}_{\rm c}$, $\hat{p}_{\rm c}$ represents the discrete boson DOF whose frequency is $\omega_{\rm c}$; ζ is the coupling constant; and the last term characterizes the bath DOF (with conjugated coordinate-momentum pairs \hat{q}_{j} , \hat{p}_{j}) interacting with the discrete boson, ξ is a homogeneous coefficient. We also assume the bath as well as its interaction with the discrete boson can be described by the spectral density function defined as below, ³⁶

$$J_{c}(\omega) = \frac{\pi}{2} \sum_{j} \frac{\tilde{c}_{j}^{2}}{\tilde{\omega}_{j}} \delta(\omega - \tilde{\omega}_{j}). \tag{C2}$$

Denoting $V'(q_s) = \partial V(q_s)/\partial q_s$, then the classical equations of motion with respect to the Hamiltonian in Eq. C1 read as

$$M_{\rm s}\ddot{q}_{\rm s} = -V'(q_{\rm s}) - \omega_{\rm c}^2 \zeta(q_{\rm c} + \zeta q_{\rm s}), \tag{C3a}$$

$$\ddot{q}_{c} = -\omega_{c}^{2}(q_{c} + \zeta q_{s}) + \sum_{j} (\xi \tilde{c}_{j} \tilde{q}_{j} - q_{c} \frac{\xi^{2} \tilde{c}_{j}^{2}}{\tilde{\omega}_{j}^{2}}), \quad (C3b)$$

$$\ddot{q}_j = -\tilde{\omega}_j^2 \tilde{q}_j + \xi \tilde{c}_j q_c. \tag{C3c}$$

Applying Fourier transform to Eq. C3 leads to

$$(-M_{\rm s}\omega^2 + \omega_{\rm c}^2\zeta^2)q_{\rm s}(\omega) + \omega_{\rm c}^2\zeta q_{\rm c}(\omega) = -V_{\omega}'(q_{\rm s}), \qquad \text{(C4a)}$$

$$\left[(\omega_{\rm c}^2 - \omega^2) + \sum_j \frac{\xi^2\tilde{c}_j^2}{\tilde{\omega}_j^2}\right]q_{\rm c}(\omega) - \sum_j \xi\tilde{c}_j\tilde{q}_j(\omega) + \omega_{\rm c}^2\zeta q_{\rm s}(\omega) = 0,$$
(C4b)

$$(\tilde{\omega}_i^2 - \omega^2)\tilde{q}_j(\omega) - \xi \tilde{c}_j q_c(\omega) = 0, \tag{C4c}$$

where $V'_{\omega}(q_s)$ is the Fourier transform of $V'(q_s)$. Plugging Eq. C4c into C4b to cancel the $\tilde{q}_j(\omega)$ terms, one obtains

$$\[\left[(\omega_c^2 - \omega^2) - \omega^2 \sum_j \frac{\xi^2 \tilde{c}_j^2}{\tilde{\omega}_j^2 (\tilde{\omega}_j^2 - \omega^2)} \right] q_c(\omega) + \omega_c^2 \zeta q_s(\omega) = 0.$$
(C5)

Further define

$$L(\omega) = -\omega^2 \left[1 + \sum_j \frac{\xi^2 \tilde{c}_j^2}{\tilde{\omega}_j^2 (\tilde{\omega}_j^2 - \omega^2)} \right], \quad (C6)$$

Eq. C5 becomes

$$q_{\rm c}(\omega) = \frac{-\omega_{\rm c}^2 \zeta q_{\rm s}(\omega)}{\omega_{\rm c}^2 + L(\omega)}.$$
 (C7)

Plugging Eq. C7 into C4a, one obtains

$$K(\omega)q_{\rm s}(\omega) \equiv \left[-M_{\rm s}\omega^2 + \frac{\omega_{\rm c}^2\zeta^2L(\omega)}{\omega_{\rm c}^2 + L(\omega)} \right] q_{\rm s}(\omega) = -V_{\omega}'(q_{\rm s})$$
(C8)

Note that Eq. C6 can be re-expressed as

$$L(\omega) = -\omega^2 \left[1 + \xi^2 \int_0^\infty ds \frac{\sum_j \frac{\tilde{c}_j^2}{\tilde{\omega}_j} \delta(s - \tilde{\omega}_j)}{s(s^2 - \omega^2)} \right]$$
$$= -\omega^2 \left[1 + \frac{2\xi^2}{\pi} \int_0^\infty ds \frac{J_c(s)}{s(s^2 - \omega^2)} \right], \quad (C9)$$

where Eq. C2 defines the loss spectral density function. The effective spectral density function is given by the branch cut of K(z) on the complex plane, reading as

$$J_{\text{eff}}(\omega) = \lim_{\epsilon \to 0^{+}} \text{Im}[K(\omega - i\epsilon)], \quad (C10)$$

which leads to 39,43

$$J_{\text{eff}}(\omega) \equiv \frac{\pi}{2} \sum_{j} \frac{\tilde{C}_{j}^{2}}{\tilde{\Omega}_{j}} \delta(\omega - \tilde{\Omega}_{j})$$

$$= \frac{\zeta^{2} \xi^{2} \omega_{c}^{4} J_{c}(\omega)}{\left[\omega_{c}^{2} - \omega^{2} + \tilde{R}(\omega)\right]^{2} + \left[\xi^{2} J_{c}(\omega)\right]^{2}}, \quad (C11)$$

where

$$\tilde{R}(\omega) = \frac{2\xi^2 \omega^2}{\pi} \mathcal{P} \int_0^\infty ds \, \frac{J_c(s)}{s(\omega^2 - s^2)}.$$
 (C12)

For the light-matter interaction Hamiltonian of Eq. 2 in the main text, one has $\xi=1$ and $\zeta=\sqrt{2\eta_{\rm c}^2/\omega_{\rm c}}$, then Eq. 11 and 12 are recovered. The effective Hamiltonian can be derived via direct normal mode transformation. ^{39,40}

Appendix D: Derivation of the τ_c expression in Eq. 31

The loss Hamiltonian is written as (cf. Eq. 5)

$$\hat{H}_{c} = \frac{1}{2} \sum_{j} \left[\hat{\tilde{p}}_{j}^{2} + \tilde{\omega}_{j}^{2} \left(\hat{\tilde{x}}_{j} - \frac{\tilde{c}_{j}}{\tilde{\omega}_{j}^{2}} \hat{q}_{c} \right)^{2} \right],$$

where the interaction term between the cavity and the photon-loss bath in the Hamiltonian above reads as

$$\hat{H}_{\rm int} = \hat{q}_{\rm c} \otimes \hat{F}_{\rm c}, \quad \hat{F}_{\rm c} \equiv \sum_{j} \tilde{c}_{j} \hat{x}_{j}.$$
 (D1)

In the second-quantization representation, Eq. D1 is expressed as

$$\hat{H}_{\rm int} = \frac{1}{\sqrt{2\omega_{\rm c}}} (\hat{a} + \hat{a}^{\dagger}) \otimes \sum_{j} \frac{\tilde{c}_{j}}{\sqrt{2\tilde{\omega}_{j}}} (\hat{\tilde{b}}_{j} + \hat{\tilde{b}}_{j}^{\dagger}), \quad (D2)$$

where
$$\hat{\tilde{x}}_j = (1/\sqrt{2\tilde{\omega}_j})(\hat{\tilde{b}}_j + \hat{\tilde{b}}_j^{\dagger}).$$

Here we take the photon number $n_{\rm ph}=1$, such that $\langle n_{\rm ph}|\hat{a}^{\dagger}|n_{\rm ph}-1\rangle=1$. We further define the Bose-Einstein distribution functions $n_{\rm b,\it j}(\tilde{\omega}_{\it j})$ as follows,

$$\sum_{n_{\mathrm{b},j}} \frac{e^{-n_{\mathrm{b},j}\beta\tilde{\omega}_{j}}}{\mathcal{Z}_{\mathrm{b}}} (n_{\mathrm{b},j}+1) \equiv n_{\mathrm{b},j}(\tilde{\omega}_{j}) + 1 = 1/(1 - e^{-\beta\tilde{\omega}_{j}}),$$

where $n_{b,j}$ denotes the phonon number of the *j*-th bath mode, and \mathcal{Z}_b is the partition function of the photon-loss bath. According to FGR, the photon loss rate can be expressed as

$$\Gamma_{c} = 2\pi \sum_{j} \sum_{n_{b,j}} \frac{e^{-n_{b,j}\beta\tilde{\omega}_{j}}}{\mathcal{Z}_{b}} \cdot |\langle n_{ph}, n_{b,j} | \hat{H}_{int} | n_{ph} - 1, n_{b,j} + 1 \rangle|^{2} \cdot \delta(\tilde{\omega}_{j} - \omega_{c})$$

$$= 2\pi \times \frac{1}{2\omega_{c}} \sum_{j} \sum_{n_{b,j}} \frac{e^{-n_{b,j}\beta\tilde{\omega}_{j}}}{\mathcal{Z}_{b}} \cdot \frac{\tilde{c}_{j}^{2}}{2\tilde{\omega}_{j}} |\langle n_{ph}, n_{b,j} | \hat{a}^{\dagger} \hat{b}_{j} | n_{ph} - 1, n_{b,j} + 1 \rangle|^{2} \cdot \delta(\tilde{\omega}_{j} - \omega_{c})$$

$$= \frac{1}{\omega_{c}} \cdot \frac{\pi}{2} \sum_{j} \frac{\tilde{c}_{j}^{2}}{\tilde{\omega}_{j}} \delta(\tilde{\omega}_{j} - \omega_{c}) \cdot \sum_{n_{b,j}} \frac{e^{-n_{b,j}\beta\tilde{\omega}_{j}}}{\mathcal{Z}_{b}} (n_{b,j} + 1) = \frac{J_{c}(\omega_{c})}{\omega_{c}(1 - e^{-\beta\omega_{c}})}, \tag{D3}$$

where we have used the definition of the loss spectral density function (Eq. 6b). Eq. D3 is the result of Eq. 31 in the main text. This rate also coincides with the Redfield rate constant for state-to-state transitions. 86,88,99,100 On the other hand, under the condition that $\tilde{R}(\omega)$ is relatively small (cf. Eq. 11),

$$J_{\text{eff}}(\omega) \approx \frac{2\eta_{\text{c}}^2 \omega_{\text{c}}^3 \Gamma_{\text{c}}(\omega) \omega}{(\omega_{\text{c}}^2 - \omega^2)^2 + \Gamma_{\text{c}}^2(\omega) \omega^2},$$
 (D4)

where $\Gamma_{\rm c}(\omega) = J_{\rm c}(\omega)/\omega$, coinciding with the friction kernel definition in the frequency domain in quantum Langevin dynamics.⁵⁰ Comparing Eq. D4 to Eq. 14, we further assume $\gamma_{\rm c}$ is large so that $\Gamma_{\rm c}(\omega)/\omega_{\rm c}$ does not change drastically in frequency, so that it can be approximated via $\Gamma_{\rm c}(\omega \to \omega_{\rm c})$, plus the detailed balance relation, then Eq. D3 is also recovered.

Appendix E: Rabi-splitting and the Fock State Description

Denoting $|\nu_{\rm L}\rangle$ as the ground vibrational state of the reactant (left well), and $|\nu'_{\rm L}\rangle$ as the first excited vibrational state of the reactant (see Sec. II C for details of these states), and $|0\rangle$ and $|1\rangle$ as the Fock state of the cavity. The light-matter interaction term is expressed as ^{17,101}

$$\hat{H}_{LM} = \sqrt{2\omega_{c}}\chi\hat{q}_{c}\mu(\hat{R}) \tag{E1}$$

$$= \sqrt{2\omega_{c}}\chi \cdot \sqrt{\frac{1}{2\omega_{c}}}(\hat{a} + \hat{a}^{\dagger}) \cdot \mu_{LL'}(|\nu_{L}\rangle\langle\nu'_{L}| + |\nu'_{L}\rangle\langle\nu_{L}|)$$

$$= \chi\mu_{LL'}(\hat{a} + \hat{a}^{\dagger}) \cdot (\hat{\sigma}^{-} + \hat{\sigma}^{+}),$$

where we have defined the raising and lowering operators as $\hat{\sigma}^- = |\nu_{\rm L}\rangle\langle\nu_{\rm L}'|$, and $\hat{\sigma}^+ = |\nu_{\rm L}'\rangle\langle\nu_{\rm L}|$. The transition dipole matrix element is defined as $\mu_{\rm LL'} = \langle\nu_{\rm L}|\mu(\hat{R})|\nu_{\rm L}'\rangle$. For the model system, we have assumed the linear dipole approximation $\hat{\mu}(\hat{R}) \approx \hat{R}$ (see Appendix A), which means $\mu_{\rm LL'} = \Delta_x$ (see Eq. A5). At the resonant condition of $\omega_{\rm c} = \omega_0$, one can make the rotating wave approximation (by ignoring counter rotating wave terms $\hat{a}^{\dagger}\hat{\sigma}^+$ and $\hat{a}\hat{\sigma}^-$) in Eq. E1, and the light-matter interaction becomes $\hat{H}_{\rm LM} = \chi \mu_{\rm LL'}(\hat{a}^{\dagger}\hat{\sigma}^- + \hat{a}\hat{\sigma}^+)$. The photon-vibration interaction couples the photon-dressed states $|\nu_{\rm L}\rangle \otimes |1\rangle$ (photonic excitation) and $|\nu_{\rm L'}'\rangle \otimes |0\rangle$ (vibrational excitation),

leading to two polariton states,

$$|\pm\rangle = \frac{1}{\sqrt{2}}[|\nu_{\rm L}\rangle \otimes |1\rangle \pm |\nu_{\rm L}'\rangle \otimes |0\rangle],$$
 (E2)

which are often referred to as the upper polariton $|+\rangle$ and lower polariton $|-\rangle$ states (which are light-matter entangled states). The energy splitting between these two polariton states is referred to as the Rabi splitting $\Omega_{\rm R}$, expressed as follows 17,101

$$\Omega_{\rm R} = 2\chi \mu_{\rm LL'} = 2\eta_{\rm c}\omega_{\rm c}\mu_{\rm LL'} \equiv 2\omega_{\rm c} \cdot \eta,$$
 (E3)

where the normalized coupling strength $\eta = \chi \mu_{\rm LL'}/\omega_{\rm c}$ characterizes the light-matter coupling strength. The Rabi splitting is often measured from the experimental transmission spectra of molecular vibrations.^{1,4} Note that the above relation between $\Omega_{\rm R}$ and η only holds under the linear approximation of the dipole operator and breaks down for the ultra-strong coupling (USC) regime^{102,103} when $\eta > 0.1$.

The Rabi splitting with respect to the model we considered here can also be evaluated via Eq. E3, e.g., for the largest coupling strength $\eta_{\rm c}=0.1$ and under resonance condition ($\omega_{\rm c}=\omega_0$), $\Omega_{\rm R}=2\eta_{\rm c}\omega_{\rm c}\mu_{\rm LL'}\approx 50.2~{\rm cm}^{-1}$, which is a typical experimental value.^{1,4} In terms of the Rabi splitting, the FGR expression in Eq. 44 can be expressed as follows

$$k_{\rm VSC} \approx \Omega_{\rm R}^2 \cdot \frac{\alpha \omega_{\rm c} \omega_0}{(\omega_{\rm c}^2 - \omega_0^2)^2 + \alpha^2 \omega_0^2} \cdot n(\omega_0).$$
 (E4)

Note that the energy unit of the coupling in the above expression is $\Omega_{\rm R}$. The regime for the FGR to be valid is often when $\Omega_{\rm R} \ll k_{\rm B}T$.

In Ref. 25 both \hat{R} and $\hat{q}_{\rm c}$ have been treated as the quantum subsystem, only \hat{H}_{ν} and $\hat{H}_{\rm c}$ are described as the environment. Because the subsystem has both vibrational and photonic DOF, one can also interpret the mechanism from the photon-dressed vibrational basis, ²⁵ in which there are mainly three types of states involved: $|\nu_{\rm L}\rangle\otimes|0\rangle$ (the ground vibrational state with 0 photons), $|\nu_{\rm L}\rangle\otimes|1\rangle$ (the ground vibrational state with 1 photon), $|\nu_{\rm L}'\rangle\otimes|0\rangle$ (the excited vibrational state with 0 photons), and accordingly, the photon dressed states for the right well. Inside the cavity, the thermal fluctuation of the cavity mode can promote $|\nu_{\rm L}\rangle\otimes|0\rangle\rightarrow|\nu_{\rm L}\rangle\otimes|1\rangle$ transition

(gaining thermal photon population). Then, a transition $|\nu_{\rm L}\rangle\otimes|1\rangle\rightarrow|\nu_{\rm L}'\rangle\otimes|0\rangle$ will occur through the light-matter coupling term (Eq. E1), which will happen efficiently if and only if the energy of these two states are resonant, explaining both resonance effects of the rate profile and the resonance condition for observing Rabi splitting (Eq. E3). Then through the tunneling splitting Δ' , the transition $|\nu_{\rm L}'\rangle\otimes|0\rangle\rightarrow|\nu_{\rm R}'\rangle\otimes|0\rangle$ will occur, and eventually leading to a faster population grown of $|\nu_R\rangle \otimes |0\rangle$. In this work, we view the photonic DOF \hat{q}_{c} to play a similar role as "RPV mode", such that it enhances the activation process of $|\nu_L\rangle \rightarrow |\nu_L'\rangle$, which eventually leads to the enhanced product population $P_{\mathcal{P}}(t)$. Because the cavity mode frequency $\omega_{\rm c}$ needs to match the $|\nu_{\rm L}\rangle \rightarrow |\nu'_{\rm L}\rangle$ transition, the rate enhancement will be very sensitive to $\omega_{\rm c}$, explaining the resonance effect of the VSC experiments. Note there is an interesting fact that because the cavity mode is purely harmonic (Eq. 2), the frequency $\omega_{\rm c}$ appeared in the Hamiltonian is identical to the frequency for the photonic state transition $|0\rangle \rightarrow |1\rangle$. This is in contrast to the molecular system, where the quantum transition frequency ω_0 (Eq. 25) is not identical to the classical bottom-well frequency $\omega_0^{\rm cl}$ (Eq. 26) when the potential is anharmonic.

- ¹A. Thomas, J. George, A. Shalabney, M. Dryzhakov, S. J. Varma, J. Moran, T. Chervy, X. Zhong, E. Devaux, C. Genet, J. A. Hutchison, and T. W. Ebbesen, "Ground-state chemical reactivity under vibrational coupling to the vacuum electromagnetic field," Angew. Chem. Int. Ed. 55, 11462–11466 (2016).
- ²R. M. A. Vergauwe, A. Thomas, K. Nagarajan, A. Shalabney, J. George, T. Chervy, M. Seidel, E. Devaux, V. Torbeev, and T. W. Ebbesen, "Modification of enzyme activity by vibrational strong coupling of water," Angew. Chem. Int. Ed. 58, 15324– 15328 (2019).
- ³ A. Thomas, A. Jayachandran, L. Lethuillier-Karl, R. M. Vergauwe, K. Nagarajan, E. Devaux, C. Genet, J. Moran, and T. W. Ebbesen, "Ground state chemistry under vibrational strong coupling: dependence of thermodynamic parameters on the rabi splitting energy," Nanophotonics 9, 249–255 (2020).
- ⁴J. Lather, P. Bhatt, A. Thomas, T. W. Ebbesen, and J. George, "Cavity catalysis by cooperative vibrational strong coupling of reactant and solvent molecules," Angew. Chem. Int. Ed. 58, 10635–10638 (2019).
- ⁵ J. Lather, A. N. K. Thabassum, J. Singh, and J. George, "Cavity catalysis: modifying linear free-energy relationship under cooperative vibrational strong coupling," Chem. Sci. 13, 195–202 (2022).
- ⁶A. Thomas, L. Lethuillier-Karl, K. Nagarajan, R. M. A. Vergauwe, J. George, T. Chervy, A. Shalabney, E. Devaux, C. Genet, J. Moran, and T. W. Ebbesen, "Tilting a ground-state reactivity landscape by vibrational strong coupling," Science 363, 615–619 (2019).
- ⁷K. Hirai, J. A. Hutchison, and H. Uji-i, "Recent progress in vibropolaritonic chemistry," ChemPlusChem 85, 1981–1988 (2020).
- ⁸T. W. Ebbesen, "Hybrid light-matter states in a molecular and material science perspective," Acc. Chem. Res. 49, 2403–2412 (2016).
- ⁹X. Li, A. Mandal, and P. Huo, "Theory of mode-selective chemistry through polaritonic vibrational strong coupling," J. Phys. Chem. Lett. **12**, 6974–6982 (2021).
- ¹⁰J. A. Campos-Gonzalez-Angulo, Y. R. Poh, M. Du, and J. Yuen-Zhou, "Swinging between shine and shadow: Theoretical advances on thermally-activated vibropolaritonic chemistry (a perspective)," (2023), arXiv:2212.04017 [physics.chem-ph].

- ¹¹J. A. Campos-Gonzalez-Angulo, R. F. Ribeiro, and J. Yuen-Zhou, "Resonant catalysis of thermally activated chemical reactions with vibrational polaritons," Nat. Commun. **10**, 4685 (2019).
- ¹²i. Vurgaftman, B. S. Simpkins, A. D. Dunkelberger, and J. C. Owrutsky, "Negligible effect of vibrational polaritons on chemical reaction rates via the density of states pathway," J. Phys. Chem. Lett. 11, 3557–3562 (2020).
- ¹³M. Du and J. Yuen-Zhou, "Catalysis by dark states in vibropolaritonic chemistry," Phys. Rev. Lett. **128**, 096001 (2022).
- ¹⁴ J. A. Campos-Gonzalez-Angulo and J. Yuen-Zhou, "Polaritonic normal modes in transition state theory," J. Chem. Phys. **152** (2020), 10.1063/5.0007547.
- ¹⁵V. P. Zhdanov, "Vacuum field in a cavity, light-mediated vibrational coupling, and chemical reactivity," Chem. Phys. **535**, 110767 (2020).
- ¹⁶T. E. Li, A. Nitzan, and J. E. Subotnik, "On the origin of ground-state vacuum-field catalysis: Equilibrium consideration," J. Chem. Phys. **152**, 234107 (2020).
- ¹⁷J. Galego, C. Climent, F. J. Garcia-Vidal, and J. Feist, "Cavity casimir-polder forces and their effects in ground-state chemical reactivity," Phys. Rev. X 9, 021057 (2019).
- ¹⁸R. F. Grote and J. T. Hynes, "The stable states picture of chemical reactions. ii. rate constants for condensed and gas phase reaction models," J. Chem. Phys. **73**, 2715–2732 (1980).
- ¹⁹P. Hänggi, P. Talkner, and M. Borkovec, "Reaction-rate theory: fifty years after kramers," Rev. Mod. Phys. **62**, 251–341 (1990).
- ²⁰S. C. Tucker, M. E. Tuckerman, B. J. Berne, and E. Pollak, "Comparison of rate theories for generalized langevin dynamics," J. Chem. Phys. 95, 5809–5826 (1991).
- ²¹X. Li, A. Mandal, and P. Huo, "Cavity frequency-dependent theory for vibrational polariton chemistry," Nat. Commun. 12, 1315 (2021).
- ²²A. Mandal, X. Li, and P. Huo, "Theory of vibrational polariton chemistry in the collective coupling regime," J. Chem. Phys. 156, 014101 (2022).
- ²³L. P. Lindoy, A. Mandal, and D. R. Reichman, "Resonant cavity modification of ground-state chemical kinetics," J. Phys. Chem. Lett. 13, 6580–6586 (2022).
- ²⁴P.-Y. Yang and J. Cao, "Quantum effects in chemical reactions under polaritonic vibrational strong coupling," J. Phys. Chem. Lett. 12, 9531–9538 (2021).
- ²⁵L. P. Lindoy, A. Mandal, and D. R. Reichman, "Quantum dynamical effects of vibrational strong coupling in chemical reactivity," Nat. Commun. 14, 2733 (2023).
- ²⁶C. Schfer, J. Flick, E. Ronca, P. Narang, and A. Rubio, "Shining light on the microscopic resonant mechanism responsible for cavity-mediated chemical reactivity," Nat. Commun. 13, 7817 (2021).
- ²⁷M. R. Fiechter, J. E. Runeson, J. E. Lawrence, and J. O. Richardson, "How quantum is the resonance behavior in vibrational polariton chemistry?" (2023), arXiv:2305.07296 [physics.chem-ph].
- ²⁸C. Cohen-Tannoudji, J. Dupont-Roc, and G. Grynberg, *Photons and Atoms: Introduction to Quantum Electrodynamics* (John Wiley & Sons, Inc., Hoboken, 1989).
- $^{29}{\rm Y.}$ Tanimura, "Nonperturbative expansion method for a quantum system coupled to a harmonic-oscillator bath," Phys. Rev. A $\bf 41,\,6676-6687$ (1990).
- ³⁰Y. Tanimura, "Stochastic liouville, langevin, fokkerplanck, and master equation approaches to quantum dissipative systems," J. Phys. Soc. Jpn. **75**, 082001 (2006).
- ³¹Y. Yan, "Theory of open quantum systems with bath of electrons and phonons and spins: Many-dissipaton density matrixes approach," J. Chem. Phys. **140**, 054105 (2014).
- ³²Y. Tanimura, "Numerically exact approach to open quantum dynamics: The hierarchical equations of motion (heom)," J. Chem. Phys. **153**, 020901 (2020).
- ³³J. P. Philbin, Y. Wang, P. Narang, and W. Dou, "Chemical reactions in imperfect cavities: Enhancement, suppression, and

- resonance," J. Phys. Chem. C 126, 14908-14913 (2022).
- ³⁴J. Flick, M. Ruggenthaler, H. Appel, and A. Rubio, "Atoms and molecules in cavities, from weak to strong coupling in quantumelectrodynamics (qed) chemistry," Proc. Natl. Acad. Sci. U.S.A. **114**, 3026–3034 (2017).
- ³⁵C. Schäfer, M. Ruggenthaler, and A. Rubio, "Ab initio nonrelativistic quantum electrodynamics: Bridging quantum chemistry and quantum optics from weak to strong coupling," Phys. Rev. A 98, 043801 (2018).
- $^{36}\mathrm{A.}$ Caldeira and A. Leggett, "Quantum tunnelling in a dissipative system," Ann. Phys. 149, 374-456 (1983).
- ³⁷At equilibrium position of the reactant coordinate R_0 , one can Taylor expand the dipole term as $\mu(R) \approx \mu_0 + \mu_0'(R - R_0)$, where $\mu_0 = \mu(R_0)$ is the permanent dipole, and $\mu_0' = \frac{\partial \mu(R)}{\partial R}|_{R_0}$ is the first order derivative. The permanent dipole μ_0 can be removed by shifting the cavity field according to $\hat{q}_c + \sqrt{2/\omega_c^3}\mu_0\chi \to \hat{q}_c$, ²¹ which will only cause a constant change to the reference potential energy surface and will influence neither the dynamics nor the reaction rate constants. Similarly, we can take $R_0 = 0$ without loss of generality.
- ³⁸A. Garg, J. N. Onuchic, and V. Ambegaokar, "Effect of friction on electron transfer in biomolecules," J. Chem. Phys. 83, 4491-4503 (1985).
- ³⁹M. Thoss, H. Wang, and W. H. Miller, "Self-consistent hybrid approach for complex systems: Application to the spin-boson model with debye spectral density," J. Chem. Phys. 115, 2991-3005 (2001).
- ⁴⁰K. H. Hughes, C. D. Christ, and I. Burghardt, "Effective-mode representation of non-markovian dynamics: A hierarchical approximation of the spectral density. i. application to single surface dynamics," J. Chem. Phys. 131, 024109 (2009).
- ⁴¹K. H. Hughes, C. D. Christ, and I. Burghardt, "Effectivemode representation of non-markovian dynamics: A hierarchical approximation of the spectral density. ii. application to environment-induced nonadiabatic dynamics," J. Chem. Phys. **131**, 124108 (2009).
- ⁴²P. Huo, S. Bonella, L. Chen, and D. Coker, "Linearized approximations for condensed phase non-adiabatic dynamics: Multilayered baths and brownian dynamics implementation," Chemical Physics 370, 87-97 (2010).
- ⁴³J. E. Lawrence, T. Fletcher, L. P. Lindoy, and D. E. Manolopoulos, "On the calculation of quantum mechanical electron transfer rates," J. Chem. Phys. 151, 114119 (2019).
- ⁴⁴A. J. Leggett, "Quantum tunneling in the presence of an arbitrary linear dissipation mechanism," Phys. Rev. B 30, 1208-1218 (1984).
- 45 It is well-known that if the secondary bath satisfies strict Ohmic dissipation (or equivalently, taking the Markovian limit), i.e., $J_{\rm c}(\omega) = \alpha \omega \exp(-\omega/\omega_{\rm m})$ with $\omega_{\rm m} \to \infty$, then $R(\omega) \to 0$, and $J_{\mathrm{eff}}(\omega)$ reduces to the form of Eq. 14. One tricky aspect is that the integral $\int_0^\infty \omega J_c(\omega) d\omega$ (and also all higher moments) diverges, and one cannot directly use the normal mode transformation relations to obtain the frequency and coupling strength of the reaction coordinate.³⁹ In more general situations, a numerical evaluation of the effective spectral density function can be performed.
- ⁴⁶U. Weiss, Quantum Dissipation Systems (World Scientific, Singapore, 1993).
- ⁴⁷M. Topaler and N. Makri, "Quantum rates for a double well coupled to a dissipative bath: Accurate path integral results and comparison with approximate theories," J. Chem. Phys. **101**, 7500–7519 (1994).
- ⁴⁸Q. Shi, L. Zhu, and L. Chen, "Quantum rate dynamics for proton transfer reaction in a model system: Effect of the rate promoting vibrational mode," J. Chem. Phys. 135, 044505 (2011).
- ⁴⁹D. T. Colbert and W. H. Miller, "A novel discrete variable representation for quantum mechanical reactive scattering via the smatrix kohn method," J. Chem. Phys. 96, 1982–1991 (1992).
- ⁵⁰S. Mukamel, Principles of Nonlinear Optical Spectroscopy (Oxford University Press, 1995).

- $^{51}\mathrm{M}.$ A. Wilson and D. Chandler, "Molecular dynamics study of
- cyclohexane interconversion," Chem. Phys. ${\bf 149},\,11{-}20$ (1990). $^{52}{\rm R.}$ F. Grote and J. T. Hynes, "Energy diffusion-controlled reactions in solution," J. Chem. Phys. 77, 3736-3743 (1982).
- $^{53}\mathrm{D.}$ J. Nesbitt and J. T. Hynes, "Slow vibrational relaxation in picosecond iodine recombination in liquids," J. Chem. Phys. 77, 2130-2143 (1982).
- ⁵⁴J. Schroeder and J. Troe, "Elementary reactions in the gas-liquid transition range," Annu. Rev. Phys. Chem. 38, 163–190 (1987).
- $^{55}\mathrm{E.}$ Pollak, H. Grabert, and P. Hänggi, "Theory of activated rate processes for arbitrary frequency dependent friction: Solution of the turnover problem," J. Chem. Phys. 91, 4073-4087 (1989).
- $^{56}\mathrm{P.~L.}$ Walters, T. C. Allen, and N. Makri, "Direct determination of discrete harmonic bath parameters from molecular dynamics simulations," J. Comput. Chem. 38, 110-115 (2017).
- ⁵⁷Here the line width can be regarded as a homogeneous broadening effect.
- ⁵⁸B. Xiang, R. F. Ribeiro, M. Du, L. Chen, Z. Yang, J. Wang, J. Yuen-Zhou, and W. Xiong, "Intermolecular vibrational energy transfer enabled by microcavity strong light-matter coupling," Science 368, 665–667 (2020).
- $^{59}\mathrm{Y}.$ Tanimura, "Nonperturbative expansion method for a quantum system coupled to a harmonic-oscillator bath," Phys. Rev. A 41, 6676–6687 (1990).
- $^{60}\mathrm{Y}.$ Tanimura, "Stochastic liouville, langevin, fokkerplanck, and master equation approaches to quantum dissipative systems," J. Phys. Soc. Jpn. 75, 082001 (2006).
- $^{61}\mathrm{R.-X.}$ Xu, P. Cui, X.-Q. Li, Y. Mo, and Y. Yan, "Exact quantum master equation via the calculus on path integrals," J. Chem. Phys. 122, 041103 (2005).
- ⁶²R.-X. Xu and Y. Yan, "Dynamics of quantum dissipation systems interacting with bosonic canonical bath: Hierarchical equations of motion approach," Phys. Rev. E 75, 031107 (2007).
- ⁶³Q. Shi, L. Chen, G. Nan, R.-X. Xu, and Y. Yan, "Efficient hierarchical liouville space propagator to quantum dissipative dynamics," J. Chem. Phys. 130, 084105 (2009)
- $^{64}\mathrm{A.}$ Bose and N. Makri, "Non-equilibrium reactive flux: A unified framework for slow and fast reaction kinetics," J. Chem. Phys. **147**, 152723 (2017).
- 65 Often, the initial density matrix can be taken as 43,48,66,67 $\hat{\rho}(0) = \frac{1}{Z_{\rm S}^{\prime}} e^{-\beta \hat{H}_{\rm S}/2} (1 \hat{h}) e^{-\beta \hat{H}_{\rm S}/2} \otimes \frac{e^{-\beta \hat{h}_{\rm B}^{\rm eff}}}{Z_{\rm B}}, \text{ where } Z_{\rm S}^{\prime} \equiv {\rm Tr}_{\rm S}[e^{-\beta \hat{H}_{\rm S}/2} (1 \hat{h}) e^{-\beta \hat{H}_{\rm S}/2}], \text{ and } \hat{H}_{\rm S} \text{ and } \hat{h}_{\rm B}^{\rm eff} \text{ are defined in } \Gamma_{\rm S}^{\rm Eff} = 0$ Eq. 18. This initial condition is more complicated and therefore less convenient to be implemented.
- ⁶⁶H. Wang, D. E. Skinner, and M. Thoss, "Calculation of reactive flux correlation functions for systems in a condensed phase environment: A multilayer multiconfiguration time-dependent hartree approach," J. Chem. Phys. 125, 174502 (2006).
- $^{67}\mathrm{I.~R.~Craig,~M.~Thoss,}$ and H. Wang, "Proton transfer reactions in model condensed-phase environments: Accurate quantum dynamics using the multilayer multiconfiguration time-dependent hartree approach," J. Chem. Phys. 127, 144503 (2007).
- $^{68}\mathrm{L}.$ Song and Q. Shi, "Calculation of correlated initial state in the hierarchical equations of motion method using an imaginary time path integral approach," J. Chem. Phys. 143, 194106 (2015).
- 69 Y. Tanimura, "Reduced hierarchical equations of motion in real and imaginary time: Correlated initial states and thermodynamic quantities," J. Chem. Phys. 141, 044114 (2014).
- ⁷⁰W. H. Miller, S. D. Schwartz, and J. W. Tromp, "Quantum mechanical rate constants for bimolecular reactions," J. Chem. Phys. 79, 4889–4898 (1983).
- ⁷¹P. Huo, I. Miller, Thomas F., and D. F. Coker, "Communication: Predictive partial linearized path integral simulation of condensed phase electron transfer dynamics," J. Chem. Phys. **139**, 151103 (2013).
- ⁷²Unfortunately, the integral in Eq. A6 is divergent for the Drude-Lorentz spectral density, so we instead take the upper limit of the integral to be the characteristic frequency γ_{ν} of the dissipa-

- tive molecular phonon bath $J_{\nu}(\omega)$ (200 cm⁻¹, which is in line with the *low-frequency modes* that cause static disorder).
- ⁷³H. Hiura, A. Shalabney, and J. George, "A reaction kinetic model for vacuum-field catalysis based on vibrational lightmatter coupling," ChemRxiv (2019).
- ⁷⁴Z.-H. Chen, Y. Wang, X. Zheng, R.-X. Xu, and Y. Yan, "Universal time-domain prony fitting decomposition for optimized hierarchical quantum master equations," J. Chem. Phys. **156**, 221102 (2022).
- ⁷⁵E. Pollak, H. Grabert, and P. Hnggi, "Theory of activated rate processes for arbitrary frequency dependent friction: Solution of the turnover problem," J. Chem. Phys. 91, 4073–4087 (1989).
- ⁷⁶I. Medina, F. J. García-Vidal, A. I. Fernández-Domínguez, and J. Feist, "Few-mode field quantization of arbitrary electromagnetic spectral densities," Phys. Rev. Lett. **126**, 093601 (2021).
- ⁷⁷M. Hertzog, P. Rudquist, J. A. Hutchison, J. George, T. W. Ebbesen, and K. Brjesson, "Voltage-controlled switching of strong lightmatter interactions using liquid crystals," Chemistry A European Journal 23, 18166–18170 (2017).
- ⁷⁸G. Stemo, H. Yamada, H. Katsuki, and H. Yanagi, "Influence of vibrational strong coupling on an ordered liquid crystal," J. Phys. Chem. B **126**, 9399–9407 (2022).
- ⁷⁹T. E. Li, B. Cui, J. E. Subotnik, and A. Nitzan, "Molecular polaritonics: Chemical dynamics under strong light–matter coupling," Annu. Rev. Phys. Chem. **73**, 4371 (2021).
- ⁸⁰R. F. Ribeiro, "Multimode polariton effects on molecular energy transport and spectral fluctuations," Commun. Chem. 5, 48 (2022).
- ⁸¹M. Snchez-Barquilla, F. J. Garca-Vidal, A. I. Fernndez-Domnguez, and J. Feist, "Few-mode field quantization for multiple emitters," Nanophotonics 11, 4363–4374 (2022).
- ⁸²M. C. Anderson, E. J. Woods, T. P. Fay, D. J. Wales, and D. T. Limmer, "On the mechanism of polaritonic rate suppression from quantum transition paths," (2023), arXiv:2304.13024 [physics.chem-ph].
- ⁸³W. Ahn, J. F. Triana, F. Recabal, F. Herrera, and B. S. Simpkins, "Modification of ground state chemical reactivity via light-matter coherence in infrared cavities," ChemRxiv 11, 10.26434/chemrxiv-2022-wb6vs-v2 (2023).
- ⁸⁴E. Pollak, H. Grabert, and P. Hänggi, "Theory of activated rate processes for arbitrary frequency dependent friction: Solution of the turnover problem," J. Chem. Phys. **91**, 4073–4087 (1989).
- ⁸⁵ A. Troisi, A. Nitzan, and M. A. Ratner, "A rate constant expression for charge transfer through fluctuating bridges," J. Chem. Phys. 119, 5782–5788 (2003).
- ⁸⁶M. A. Castellanos and P. Huo, "Enhancing singlet fission dynamics by suppressing destructive interference between charge-transfer pathways," J. Phys. Chem. Lett. 8, 2480–2488 (2017).
- ⁸⁷S. N. Chowdhury, A. Mandal, and P. Huo, "Ring polymer quantization of the photon field in polariton chemistry," J. Chem. Phys. **154**, 044109 (2021).
- ⁸⁸V. May and O. Khn, Charge and Energy Transfer Dynamics in Molecular Systems (John Wiley & Sons, Ltd, 2011) Chap. 6,

- pp. 255–307.
- ⁸⁹T. Ozaki, "Continued fraction representation of the fermi-dirac function for large-scale electronic structure calculations," Phys. Rev. B **75**, 035123 (2007).
- ⁹⁰ J. Hu, R.-X. Xu, and Y. Yan, "Communication: Pad spectrum decomposition of fermi function and bose function," J. Chem. Phys. **133**, 101106 (2010).
- ⁹¹J. Hu, M. Luo, F. Jiang, R.-X. Xu, and Y. Yan, "Pad spectrum decompositions of quantum distribution functions and optimal hierarchical equations of motion construction for quantum open systems," J. Chem. Phys. **134**, 244106 (2011).
- ⁹²H. Liu, L. Zhu, S. Bai, and Q. Shi, "Reduced quantum dynamics with arbitrary bath spectral densities: Hierarchical equations of motion based on several different bath decomposition schemes," J. Chem. Phys. **140**, 134106 (2014).
- ⁹³C. Duan, Q. Wang, Z. Tang, and J. Wu, "The study of an extended hierarchy equation of motion in the spin-boson model: The cutoff function of the sub-ohmic spectral density," J. Chem. Phys. **147**, 164112 (2017).
- ⁹⁴Q. Wang, Z. Gong, C. Duan, Z. Tang, and J. Wu, "Dynamical scaling in the ohmic spin-boson model studied by extended hierarchical equations of motion," J. Chem. Phys. **150**, 084114 (2019).
- ⁹⁵N. Lambert, S. Ahmed, M. Cirio, and F. Nori, "Modelling the ultra-strongly coupled spin-boson model with unphysical modes," Nat. Commun. 10, 3721 (2019).
- ⁹⁶U. Mller and G. Stock, "Flow of zero-point energy and exploration of phase space in classical simulations of quantum relaxation dynamics. ii. application to nonadiabatic processes," J. Chem. Phys. 111, 77–88 (1999).
- ⁹⁷N. Makri, "The linear response approximation and its lowest order corrections: An influence functional approach," J. Phys. Chem. B **103**, 2823–2829 (1999).
- ⁹⁸L. Chen and Q. Shi, "Quantum rate dynamics for proton transfer reactions in condensed phase: The exact hierarchical equations of motion approach," J. Chem. Phys. 130, 134505 (2009).
- ⁹⁹T. C. Berkelbach, M. S. Hybertsen, and D. R. Reichman, "Microscopic theory of singlet exciton fission. II. Application to pentacene dimers and the role of superexchange," J. Chem. Phys. 138, 114103 (2013).
- ¹⁰⁰W.-L. Chan, T. C. Berkelbach, M. R. Provorse, N. R. Monahan, J. R. Tritsch, M. S. Hybertsen, D. R. Reichman, J. Gao, and X.-Y. Zhu, "The quantum coherent mechanism for singlet fission: Experiment and theory," Acc. Chem. Res. 46, 1321–1329 (2013).
- ¹⁰¹A. Shalabney, J. George, J. Hutchison, G. Pupillo, C. Genet, and T. W. Ebbesen, "Coherent coupling of molecular resonators with a microcavity mode," Nat. Commun. 6, 5981 (2015).
- ¹⁰² A. Settineri, V. Macrí, A. Ridolfo, O. Di Stefano, A. F. Kockum, F. Nori, and S. Savasta, "Dissipation and thermal noise in hybrid quantum systems in the ultrastrong-coupling regime," Phys. Rev. A 98, 053834 (2018).
- ¹⁰³A. Frisk Kockum, A. Miranowicz, S. De Liberato, S. Savasta, and F. Nori, "Ultrastrong coupling between light and matter," Nat. Rev. Phys. 1, 19–40 (2019).